

1 **In situ observations of supercooled liquid water clouds over Dome**
2 **C, Antarctica by balloon-borne sondes**

3

4 **Philippe Ricaud¹, Pierre Durand², Paolo Grigioni³, Massimo Del Guasta⁴, Giuseppe**
5 **Camporeale⁵, Axel Roy¹, Jean-Luc Attié², and John Bognar⁶**

6

7 ¹CNRM, Université de Toulouse, Météo-France, CNRS, 42, Avenue G. Coriolis
8 31057, Toulouse Cedex, France

9 ²Laboratoire d'Aérodynamique, Université de Toulouse, CNRS, UPS, 14 Avenue Edouard Belin,
10 31400, Toulouse, France

11 ³ENEA, Laboratory for Observations and Measurements for Environment and Climate, Via
12 Anguillarese, 301 00123, Rome, Italy

13 ⁴INO-CNR, Via Nello Carrara, 1 – 50019 Sesto Fiorentino, Italy

14 ⁵IREA – CNR, Via G. Amendola n. 122 D/O, 70126 Bari, Italy

15 ⁶Anasphere, Inc., 5400 Frontage Road, 59741 Manhattan, MT, USA

16

17 Correspondence: philippe.ricaud@meteo.fr

18

19

20 ~~18 March~~ 1 July 2024, Revision R01, Version ~~V00~~V03

21

22 Submitted to **Atmospheric Measurements and Techniques**

23

24

25 **Abstract**

26 Clouds in Antarctica are key elements that affect radiative forcing and thus Antarctic
27 climate evolution. Although the vast majority of clouds are composed of ice crystals, a non-
28 negligible fraction is constituted of supercooled liquid water (SLW, water held in liquid form
29 below 0°C). Numerical weather prediction models have a great difficulty to forecast SLW
30 clouds over Antarctica favouring ice at the expense of liquid water, and therefore incorrectly
31 estimating the cloud radiative forcing. Remote sensing observations of SLW clouds have been
32 carried out for several years at Concordia station (75°S, 123°E, 3233 m above mean sea level),
33 combining active LIDAR measurements (SLW cloud detection) and passive HAMSTRAD
34 microwave measurements (liquid water path, LWP). The present project aimed at in situ
35 observations of SLW clouds using sondes developed by the company Anasphere, specifically
36 designed for SLW content (SLWC) measurements. These SLWC sondes were coupled to
37 standard meteorological pressure-temperature-humidity sondes from the Vaisala Company and
38 released under meteorological balloons. During the 2021-2022 summer campaign, 15 launches
39 were made, of which 7 were scientifically exploitable a- Above a height of 400 m above ground
40 level, a threshold height imposed by the time the SLWC sonde takes to stabilize after the launch.
41 The three main outcomes from our analyses are: a) the first in-situ observations of SLW clouds
42 so far in Antarctica with SLWC sondes; b) on average, the consistency of SLW cloud heights
43 as observed by in-situ sondes and remote-sensing LIDAR; and c) Liquid Water Path (vertically-
44 integrated SLWC) deduced by the sondes being generally equal or greater than LWP remotely
45 sensed by HAMSTRAD. we found that the SLWC sondes detected SLW clouds in a vertical
46 range consistent with LIDAR observations. In nominal operation, the LWP values obtained
47 either by HAMSTRAD or vertically integrated from the SLWC sonde profiles were consistent
48 in spite of their low values ($< 10 \text{ g m}^{-2}$). On some occasions far from nominal operation (surface
49 fog, low vertical ascent of the balloon), the LWPs from the SLWC sonde were overestimated

Mis en forme : Retrait : Première ligne : 0,75 cm

50 ~~by a factor of 5-10 compared to the HAMSTRAD values.~~ In general, the SLW clouds were
51 observed in a layer close to saturation ($U > 80\%$) or saturated ($U \sim 100-105\%$) just below or at
52 the lowermost part of the entrainment zone or capping inversion zone which exists at the top of
53 the Planetary Boundary Layer and is characterized by an inflection point in the potential
54 temperature vertical profiles. Our results are consistent with the theoretical view that SLW
55 clouds form and pertain at the top of the Planetary Boundary Layer.

Mis en forme : Anglais (États-Unis)

56 **1. Introduction**

57 Clouds in Antarctica are key parameters that affect the Earth radiative balance thus the
58 climate evolution over Antarctica but also over the Earth through complex teleconnections
59 (Lubin et al., 1998). The nature of the clouds (ice or liquid or mixed phase, a mixture of liquid
60 and solid water) and their vertical distributions together with their interactions with aerosols
61 add complexity to this topic. Numerical simulations at local or global scales, focused on short
62 time scales or climate evolution show large differences between clouds located above the
63 Southern Ocean, the Western Antarctica – and particularly the Antarctic Peninsula –, the
64 Eastern Antarctic Plateau and *in fine* Antarctic coastal areas (see e.g. Fogt and Bromwich,
65 2008). In general, ice clouds are relatively well estimated by ~~the weather~~ models while
66 supercooled liquid water (SLW) clouds tend to be underestimated because the water partition
67 function favours solid instead of liquid phase for temperature less than 0°C (see e.g. Ricaud et
68 al., 2020). This flaw is rather observed in global-scale models but could be reduced in models
69 including a detailed microphysics scheme (e.g. Engdahl et al., 2020). Therefore, the impact of
70 the clouds on the net surface radiation, the so-called cloud radiative forcing, that strongly
71 depends on the nature of the cloud, is usually underestimated by 5-30 W m⁻² in models that
72 favour ice instead of SLW clouds (King et al., 2006, 2015; Bromwich et al., 2013; Lawson and
73 Gettelman, 2014; Listowski and Land-Cope, 2017; Young et al., 2019). From observations and
74 climate models, it appears that, in Antarctica, the liquid water path (LWP), which is the
75 vertically-integrated SLW content (SLWC), is on average less than 10 g m⁻², with slightly larger
76 values in summer than in winter by 2-5 g m⁻² (Lenaerts et al., 2017), whereas, in the Arctic,
77 values greater than 50 g m⁻² were reported (Lemus et al., 1997; Zhang et al., 2019) and, at
78 middle/tropical latitudes, values ranging 100-150 g m⁻² were measured and ~~modelled-simulated~~
79 (Lemus et al., 1997).

Mis en forme : Police :Italique

80 In parallel, cloud observations over Antarctica are difficult because of the very small
81 number of ground stations which are located preferably near the coast with only three of them
82 opened all year-long deep inside the continent. It is the reason why space-borne measurements
83 are paramount to classify clouds over the entire continent as a function of height, nature, and
84 time. It is clearly accepted now that SLW clouds are much more abundant near the coast than
85 in the inner continent (Bromwich et al., 2012; Listowski et al., 2019) with larger ice crystals
86 and water droplets (Lachlan-Cope, 2010; Lachlan-Cope et al., 2016; Grosvenor et al., 2012;
87 O'Shea et al., 2017; Grazioli et al., 2017) and that the cloud radiative forcing is maximum over
88 the Antarctic Peninsula with values reaching 40 W m^{-2} (Ricaud et al., 2024). In addition to this
89 continent-scale information provided by satellites, it is crucial to obtain information at the local
90 scale from remote and/or in situ observations. Remote observations of SLW/mixed phase cloud
91 are usually performed by means of backscattered LIDARs and ceilometers while in situ
92 observations have been performed over the Southern Ocean (Chubb et al., 2013), Western
93 Antarctica (Grosvenor et al., 2012; Laclan-Cope et al., 2016) and coastal areas (O'Shea et al.,
94 2017) using instruments on-board aircraft.

95 At Concordia station, several studies from remote-sensed observations already took place
96 to evaluate: 1) the presence of the SLW/mixed phase clouds over the station mainly based on a
97 backscattered LIDAR (Cossich et al., 2021), 2) the amount of the LWP within SLW clouds
98 (Ricaud et al., 2020), 3) the impact of SLW clouds on the net surface radiation (Ricaud et al.,
99 2020), 4) the differences between observations and model simulations of SLW clouds (Ricaud
100 et al., 2020), 5) the relationship between in-cloud temperature and LWP (Ricaud et al., 2024),
101 and 6) the relationship between LWP and cloud radiative forcing (Ricaud et al., 2024). In
102 general, SLW clouds are preferably observed in summer with very small LWPs ($< 10 \text{ g m}^{-2}$),
103 in-cloud temperatures ranging from -20°C to -38°C and a cloud radiative forcing up to a
104 maximum value of 40 W m^{-2} (Ricaud et al., 2024).

105 We have thus proposed a new project to observe SLW clouds in situ at Concordia, based
106 on the use of a sonde developed by the Anasphere ~~Company~~ company and especially designed
107 for the detection of this type of cloud. During the summer campaign 2021-2022, the SLWC
108 sonde was connected to a standard Vaisala pressure-temperature-humidity (PTU) sonde and
109 embarked under an ascending balloon while, during the summer campaign 2022-2023, the two
110 coupled sondes were installed aboard a vertical take-off and landing (VTOL) drone. Numerous
111 SLW clouds were present during the 2021-2022 campaign while, in 2022-23, they were very
112 scarce over the station with a net consequence of measuring only vertical profiles of temperature
113 and relative humidity (Ricaud et al., 2023).

114 The aim of the present study was to perform for the first time in-situ observations of SLW
115 clouds above the Concordia station during the summer campaign 2021-2022. For the validation
116 and interpretation of the data, we relied on the observations performed by 1) the backscatter
117 LIDAR installed at the station for more than ten years to characterize the nature of the clouds
118 (ice/liquid/mixed phase) and ~~its~~ their height and 2) the LWPs measured by the HAMSTRAD
119 microwave radiometer set up at the station in 2009.

120 The article is structured as follows. The instruments are presented in Sect. 2. The
121 methodology is explained in Sect. 3. The results of the campaign are presented in Sect. 4 before
122 being synthetized and discussed in Sect. 5. A conclusion finalizes the findings in Sect. 6. Note
123 that all the observations performed during the summer campaign are presented in a companion
124 document as supplementary materials.

125

126 **2. Instruments**

127 In addition to the Vaisala PTU and Anasphere SLWC sondes attached to the meteorological
128 balloons, we used observations from two other instruments installed at the Concordia station

129 for several years, namely the backscatter LIDAR to classify the cloud as an SLW cloud, and
130 the HAMSTRAD microwave radiometer to obtain the LWP.

131

132

133

134 2.1. PTU sondes

135 The PTU sondes used during the 2021-2022 summer campaign were standard Vaisala RS-
136 41 SGP sondes (an upgraded version of the Vaisala's RS92 radiosondes), which are now used
137 daily at Concordia to obtain operational temperature and humidity vertical profiles at 12:00
138 UTC. The sondes were attached to the balloon with a string either unwound before launching
139 (and with a length $L = 20$ or 40 m) or wound on an unwinder. We systematically used a
140 parachute to obtain vertical profiles in both the ascending and descending phases.

141 2.2. SLWC sondes

142 The Anasphere's vibrating-wire sonde records a vibrating wire's frequency as ice
143 accumulates along its length (Serke et al., 2014). When the SLW reaches the wire, liquid
144 droplets are instantly converted into ice. These frequency measurements, combined with
145 collocated meteorological measurements, can be used to determine the SLWC of the
146 surrounding air. The SLWC sonde actually measures the frequency of the vibrating wire. Since
147 this frequency f varies according to the change in mass of the wire, its derivative with respect
148 to ~~(wrt)~~ time df/dt can be used to calculate the ~~water~~ SLWC collected by the wire, ~~either in~~
149 ~~the form of ice or absorbed liquid, depending on whether the wire in question is gel coated or~~
150 ~~nickel plated, respectively.~~ From Dexheimer et al. (2019), SLWC (g m^{-3}) is estimated to be:

$$151 \quad SLWC = -(2b_0f_0^2/\varepsilon D\omega f^3) \times (df/dt) \quad (1)$$

152 where ε is the droplet collection efficiency (~ 0.9), D is the wire diameter including the
153 hydrophilic gel (~~0.030 inch or~~ $0.762 \text{ } 10^{-3} \text{ mm}$), b_0 is the vibrating-wire mass per unit length

154 including the hydrophilic gel (2.24 g m^{-1}), ω is the velocity of air relative to the wire ($\sim 5 \text{ m s}^{-1}$) and f_0 is the un-iced wire frequency in Hertz ranging from 21.50 to 22.50 Hz during the
155 campaign. f typically ranges from 20.0 to 22.85 Hz during the campaign. Note that ω is given, irrespective of its direction (upward, downward, etc.). During the ascending phase, given that
156 the balloon has an upward buoyancy, it always rises with respect to the air parcel it is in. The
157 nominal operation of the SLWC sonde requires that it is well working with an air flow of about
158 5 m s^{-1} . It is the reason why the balloon pressure is set up for an average ascending rate (with
159 respect to the ground) of $\sim 5 \text{ m s}^{-1}$. During the descending phase, after the balloon has burst, the
160 sonde falls with a parachute with a downward buoyancy and a downward velocity relative to
161 the air parcel of about $5\text{-}6 \text{ m s}^{-1}$. The ascending rate was typically ranging $4.0\text{-}6.0 \text{ m s}^{-1}$ during
162 our launches performed at Concordia. So we can associate to ω an error (variability) of the
163 order of $\pm 1.0 \text{ m s}^{-1}$. This impacts on the SLWC calculation by $\pm 3\%$. The droplet collection
164 efficiency ε depends on the median droplet diameter d considered. In Dexheimer et al. (2019),
165 values of 11, 16 and 20 microns based on Lozowski et al. (1983) and Bain and Gayet (1982)
166 were used to calculate SLWC. A median droplet diameter of $d = 16$ microns resulted in a
167 collection efficiency greater than 0.9. This later value was finally given since it provided the
168 lower estimate of SLWC in all observations performed in the Arctic. We thus also used an
169 efficiency of 0.9 in our study. The sensitivity of ε to the median droplet diameter d has thus
170 been investigated. For d varying from 11 to 20 microns, SLWC is varying by $\pm 12\%$.

173 The output signal of the sonde is connected to the Vaisala radiosonde which transmits the
174 data to the ground station via telemetry. The observations of the two sondes are thus
175 synchronized. The integration time is 5 s, thus providing an observation every $\sim 25 \text{ m}$ along the
176 vertical. We have applied a 4-point running average to all our observations. This means that
177 our vertical profiles, even sampled every $\sim 25 \text{ m}$, are not able to describe the variations for scales
178 lower than 100 m . This means that our vertical profiles, even sampled every $\sim 25 \text{ m}$, have a

Mis en forme : Police :Italique

Mis en forme : Exposant

Mis en forme : Exposant

Mis en forme : Exposant

Mis en forme : Police :Symbol, Italique

Mis en forme : Police :Italique

Mis en forme : Police :Italique

Mis en forme : Police :Symbol, Italique

Mis en forme : Police :Italique

Mis en forme : Police :Italique

Mis en forme : Anglais (États-Unis)

179 ~~vertical definition of about 100 m.~~ Since it takes about 60-80 s from the launch for the SLWC
180 sonde to stabilize, the minimum height for meaningful observations is ~300-400 m above
181 ground level (agl), below which we are unable to detect any SLW cloud. Note that, in the
182 following, all heights are given in agl.

183 2.3. LIDAR

184 The tropospheric depolarization backscatter LIDAR (532 nm) has been operating at Dome
185 C since 2008 (see http://lidarmax.altervista.org/englidar/_Antarctic%20LIDAR.php). The
186 LIDAR provides 5-min tropospheric profiles of aerosols and clouds continuously, from 20 to
187 7000 m, with a resolution of 7.5 m. LIDAR depolarization (Mishchenko et al., 2000) is a robust
188 indicator of non-spherical shape for randomly oriented cloud particles. A depolarization ratio
189 below 10% is characteristic of SLW clouds, while higher values are produced by ice particles.
190 The potential ambiguity between SLW cloud and oriented ice plates is avoided at Dome C by
191 operating the LIDAR 4° off-zenith (Hogan and Illingworth, 2003).

192 2.4. HAMSTRAD

193 HAMSTRAD is a microwave radiometer that profiles water vapour, ~~liquid water~~ and
194 tropospheric temperature together with LWP above Dome C. Measuring at both 60 GHz
195 (oxygen molecule line (O₂) to derive the temperature) and 183 GHz (H₂O line), ~~this unique,~~
196 ~~state-of-the-art~~ radiometer was installed on site for the first time in January 2009 (Ricaud et
197 al., 2010). Measurements from the HAMSTRAD radiometer allow the retrieval of vertical
198 profiles of water vapour and temperature from the ground to 10 km altitude with vertical
199 resolutions of 30 to 50 m in the Planetary Boundary Layer (PBL), 100 m in the lower free
200 troposphere and 500 m in the upper troposphere-lower stratosphere. The LWP (g m⁻²) can also
201 be estimated. The time resolution is adjustable and fixed at 60 seconds since 2018. Note that an
202 automated internal calibration is performed every 12 atmospheric observations and takes about
203 4 minutes. Consequently, the atmospheric time sampling is 60 seconds for a sequence of 12

204 profiles, and a new sequence starts 4 minutes after the end of the previous one. The temporal
205 resolution of the instrument allows the detection of clouds and diamond dust (Ricaud et al.,
206 2017) together with the SLW clouds (Ricaud et al., 2020). The 2021-2022 and the 2022-2023
207 summer campaigns were dedicated to in-situ observations of SLW clouds using balloons and a
208 drone (Ricaud et al., 2023), respectively. Comparisons with numerical weather prediction
209 (NWP) models showed consistent amounts of LWP at Dome C when the ice-liquid water
210 partition function favours SLW for temperatures below 0°C (Ricaud et al., 2020).

211

212 3. Methodology

213 In order to optimize in-situ SLW cloud observations, we developed the following
214 procedure. 1) The remotely-sensed and real-time observations of clouds (either ice crystals
215 and/or SLW) from the LIDAR were checked regularly. 2) When the presence of SLW was
216 verified, we checked the value of LWP from HAMSTRAD. An empirical value of $LWP_0 = 1.0$
217 g m^{-2} was estimated as the threshold above which an SLW cloud is considered as significant.
218 For $LWP < LWP_0$, either the amount of liquid water in the cloud was too low or the SLW cloud
219 was too scattered. 3) If the two-above conditions were fulfilled for more than 2 hours, we started
220 the connection and calibration process of the 2 sondes (PTU and SLWC) via the Vaisala
221 Digicora station inside the Concordia station. Then we went outside and inflated the
222 meteorological balloon. Finally, we launched the 2 sondes attached to the balloon using either
223 an unwinder or an unwound string (Figure 1). In total, the step 3) lasted about 1 hour. As we
224 used standard meteorological balloons (Totex TA100), we were able to probe the atmosphere
225 from the surface up to about 12-13 km height (ascent and descent) for a total duration of about
226 1 hour and 40 minutes. Since the tropopause height was ranging 7-8 km and we were only
227 interested in the first 2 km where the SLW clouds are located, only 2-5% of the observations
228 made were scientifically sound for our project. This is the main reason why we used a drone

229 during the next campaign 2022-2023 to detect SLW clouds in the PBL (Ricaud et al., 2023).

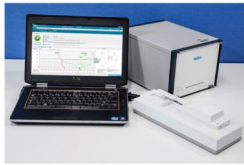
230 Note that, since there was only one Vaisala Digicora station for both our project and the

231 operational meteorological sounding at 12:00 UTC, we could not use the time window between

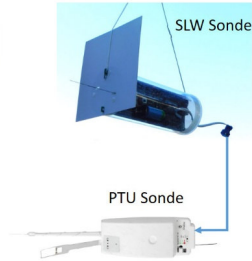
232 09:00 and 14:00 UTC for our studies.

233

1)
PTU Sonde calibration
into the station



2)
SLW Sonde coupled to
the PTU Sonde



3)
Two sondes attached to the
meteorological balloon
and launched



234



235

236 **Figure 1:** The methodology employed to launch the SLWC sonde with meteorological balloons
237 is synthetized as follow. 1) The Vaisala PTU sondes are calibrated into the quiet building of the
238 Concordia station at room temperature using the standard Digicora system. 2) The SLWC sonde
239 is connected to the PTU sonde at room temperature and then is transported outdoors to the
240 meteorological shelter. The two sondes are attached to the meteorological balloon after inflation
241 of the balloon. 3) Then, after leaving the shelter, one scientist maintains the SLWC sonde in
242 his/her hands while another one maintains both the meteorological balloon and the PTU sonde.
243 When the meteorological and technical conditions are optimised, the balloon is launched. The
244 picture represents a ~~Launch~~-launch of a Vaisala PTU sonde (left hand of the man in blue) and
245 an Anasphere SLWC sonde (right hand of the man in red) attached to the Totex TA100
246 meteorological balloon, together with the red parachute and the unwinder for the first flight on
247 22 December 2021.

248
249 In general (see e.g., Ricaud et al., 2020), SLW clouds are usually capped by a thin
250 temperature inversion and a decrease from high relative humidity $U (>80\%)$. As this inversion
251 layer separates two layers where temperature decreases with height, it contains an inflection
252 point in the temperature (or potential temperature) profile the height of which $H(T_{inf})$ can be
253 used as the top of the atmospheric boundary layer with its capping SLW cloud layer. Such a
254 definition based on the height of the inflection point is frequently used for the determination of
255 the boundary-layer thickness (Hennemuth and Lammert, 2006). Consistent with this definition,
256 Ricaud et al. (2020) adapted from Stull (2012) proposed to consider the potential temperature
257 vertical distribution profiles separating the diurnal variation of the top of the planetary boundary
258 layer into 2 phases: 1) the entrainment zone at the top of the mixed layer where the SLW cloud
259 develops and 2) the capping inversion zone under which the SLW cloud still persists at the top
260 of the residual quasi-mixed layer. The vertical limits of these two layers are well defined by the

261 height of the inflection points $H(\theta_{inf})$. In the following, we have used information from
262 profiles of the potential temperature θ (K) defined as:

$$263 \quad \theta = T(P_0/P)^{R/C_p} \quad (2)$$

264 where T is the temperature (K), P the pressure (hPa), P_0 the reference pressure (1000 hPa), R
265 the gas constant of air ($\text{J kg}^{-1} \text{K}^{-1}$) and C_p the heat capacity at constant pressure ($\text{J kg}^{-1} \text{K}^{-1}$).
266 R/C_p is taken at 0.286. We have characterized inflection points heights $H(\theta_{inf})$ in the potential
267 temperature vertical profiles when the second derivatives in θ with respect to the height z
268 ($d^2 \theta / dz^2$) are greater than an empirical threshold value typically varying from $1.5 \cdot 10^{-4}$ to 4.0
269 10^{-4} K m^{-2} .

270

271 **4. Results**

272 *4.1. Period of study*

273 The balloon-borne observations of SLW clouds were carried out during the 2021-2022
274 summer campaign at Concordia. A total of 15 launches were performed from 21 December
275 2021 to 28 January 2022 (labelled from L01 to L15, respectively). With the exception of 17
276 January 2022 (L11), when the observations were made to check the behaviour of the SLWC
277 sondes in cloud-free conditions, all other launches were made when a SLW cloud was detected
278 for more than 2 hours with the LIDAR observations using the depolarization method described
279 in section 2.3.

280 Table 1 lists all the launches that were scientifically exploitable in ascending, descending
281 or both modes [while Table 2 lists the two scientifically-exploitable launches in cloud-free](#)
282 [conditions](#). In order to avoid listing a catalogue of observations, we chose to only show details
283 and Figures relative to the launches performed on 25 December 2021 and on 17 January 2022
284 (cloud-free period). Nevertheless, the SLWC vertical [distributions-profiles](#) calculated for all the
285 flights are shown and discussed in the forthcoming sections. The information regarding all the

286 scientifically-exploitable flights are presented in the supplementary materials. This
287 encompasses: 1) the LWP values from HAMSTRAD and the height range of the SLW clouds
288 from the LIDAR over one day, 2) the profiles of temperature, potential temperature and relative
289 humidity measured by the PTU sonde during the flights, and 3) the profile of the SLWC sonde
290 frequency f , the derivative of the frequency with respect to time t (df/dt) and the calculated
291 SLWC during the flights.

292

293 **Table 1:** List of SLW cloud flights performed during the 2021-2022 season over Concordia,
294 together with date, launch time (UTC) and in *italic* the time (UTC) when the balloon hits the
295 ground after the descent, SLW cloud vertical range (m) and associated LWP (g m^{-2}) in
296 ascending (A) or descending (D) phase, considering only SLWC sonde observations above 400
297 m agl. Also shown are the SLW cloud vertical range (m) observed by the LIDAR in time
298 coincidence within ± 1 hour with the flight in ascending phase and, in *italic*, in descending phase.
299 Also presented are the minimum-maximum LWP (g m^{-2}) measured by HAMSTRAD for the
300 same date over 24 hours. Also included are: heights (m) of the inflection point in the vertical
301 profile of potential temperature $H(\theta_{inf})$, information on the type of string used (unwinder or
302 unwound string of length L), on the velocity ω when it departs significantly from the nominal
303 value of 5 m s^{-1} and on surface liquid fog when present. Heights are always given in meters agl.
304 Meteorological conditions (Meteo) encountered and synthetized as: HP=Heavy Precipitation;
305 LP=Light Precipitation; LF=Liquid Fog. **Table 1:** List of SLW cloud flights performed during
306 the 2021-2022 season over Concordia, together with date, launch time (UTC) and in *italic* the
307 time (UTC) when the balloon hits the ground after the descent, SLW cloud vertical range (m)
308 and associated LWP (g m^{-2}) in ascending (ASC) or descending (DES) phase, considering only
309 observations above 400 m agl. Also shown are the SLW cloud vertical range (m) observed by
310 the LIDAR in time coincidence with the flight and the minimum-maximum LWP (g m^{-2})

Mis en forme : Interligne : Double

311 measured by HAMSTRAD for the same date over 24 hours. Also included are: heights (m) of
 312 the inflection point in the vertical profile of potential temperature $H(\theta_{inf})$, information on the
 313 type of string used (unwinder or unwound string of length L), and any other relevant information
 314 (vertical ascent velocity ω less than the nominal 5 m s^{-1} , cloud-free period, surface fog). Heights
 315 are always given in meters agl. The root mean square error (RMSE) $\sigma (\text{g m}^{-3})$ associated with
 316 the SLWC profiles in cloud-free conditions is also estimated.

Launch A/D	Date YYMMDD	Launch Time HH:MM:SS UTC	Comments	Meteo	$H(\theta_{inf})$ m	SLW cloud vertical domain		LWP g m^{-2}	
						Sonde m	LIDAR m	Sonde	Hamstrad Min-Max
L01 A	211222	02:24:30	Unwinder	HP	710-750	400-500	400-600 700-750	7.37	2-10
L03 D	211225	08:53:15 10:30:00	Unwinder	HP	950-1000 1450-1500	900-1000 1400-1500	600-800 800-900 1100-1200	3.67	2-6
L04 A	211225	15:48:51	Unwinder	LP	850-880 1400 1520	825-875	700-900	9.08	2-6
L06 A	211229	13:45:00	$L = 40 \text{ m}$ $H > 750 \text{ m}$	LP	< 750	750-825	500-800	7.48	1.0-3.5
L07 A	211229	17:47:51	$L = 40 \text{ m}$ $\omega \sim 3.5 \text{ m/s}$	LP	700 850	425-600 750-900	600-750	33.17 23.94	1.0-3.5
L14 A	220124	13:51:05	$L = 20 \text{ m}$	LF	630 900-920 1400	600 800-1000	50-250 750-850	575.35	1-5
L14 D	220124	13:51:05 15:30:00	$L = 20 \text{ m}$	LF	810 1340 1420	775-825(*)	50-300 750-850	28.74	1-5
L15 A	220128	06:08:27	$L = 20 \text{ m}$	LP	650 910 1080	400-500 550-700 1000-1050	700-800 950-1050	17.62 13.75 7.31	2-5

317 (*) Most intense spike

318

319

320

Launch # ASC/DES	Date YYMMDD	Launch Time HH:MM:SS UTC	Comments	$H(\theta_{inf})$ m	SLW cloud vertical domain		LWP g m^{-2}	
					Sonde m	LIDAR m	Sonde	Hamstrad Min-Max
L01 ASC	211222	02:24:30	Unwinder	710-750	400-500	400-600 750	7.37	2-10
L03 DES	211225	08:53:15 10:30:00	Unwinder	950-1000 1450-1500	900-1000 1400-1500	600-800 800-1000 1200-1300	3.67	2-6

L04 ASC	211225	15:48:51	Unwinder	850-880 1400 1520	700-900 1500	700-900	9.08	2-6
L06 ASC	211229	13:45:00	$L=40\text{ m}$ $H>750\text{ m}$	<750	750-850	600-800	7.48	1.0-3.5
L07 ASC	211229	17:47:51	$L=40\text{ m}$ $w=3.5\text{ m}\cdot\text{s}^{-1}$	700 850	400-600 750-900	600-800	33.17 23.94	1.0-3.5
L14 ASC	220124	13:51:05	$L=20\text{ m}$ Fog	630 900-920 1400	600 800-1000	800	575.35	1-5
L14 DES	220124	13:51:05 15:30:00	$L=20\text{ m}$ Fog	810 1340 1420	800 1000	800	18.92	1-5
L15 ASC	220128	06:08:27	$L=20\text{ m}$	650 910 1080	600-800 1000-1100	600-800 900-1000	10.15 7.31	2-5
L11 ASC	220117	06:35:15	$L=40\text{ m}$ Cloud-Free				-0 $\sigma=0.05\text{ g}\cdot\text{m}^{-3}$	0.4-1.0
L11 DES	220117	06:35:15 08:20:00	$L=40\text{ m}$ Cloud-Free				-0 $\sigma=0.05\text{ g}\cdot\text{m}^{-3}$	0.4-1.0

321

322 **Table 2.** Flight L11 performed in cloud-free conditions during the 2021-2022 season over
323 Concordia, together with date, launch time (UTC) and in *italic* the time (UTC) when the balloon
324 hits the ground after the descent, in ascending (ASC) or descending (DES) phase. Also
325 presented are: the LWP calculated from SLWC sonde observations, the minimum-maximum
326 LWP (g m^{-2}) measured by HAMSTRAD for the same date over 24 hours, the variability σ of
327 the SLWC as calculated from the SLWC sonde observations (g m^{-3}) and of the LWP as
328 calculated from the HAMSTRAD observations (g m^{-2}). An information on the type of string
329 used (unwinder or unwound string of length L) is also provided.

Mis en forme : Interligne : Double

Launch A/D	Date YYMMDD	Launch Time HH:MM:SS UTC	Comments	LWP g m^{-2}		Variability / σ	
				Sonde	Hamstrad Min-Max	SLWC sonde g m^{-3}	LWP Hamstrad g m^{-2}
L11 A	220117	06:35:15	$L=40\text{ m}$	~0	0.4-1.0	0.08	0.2
L11 D	220117	06:35:15 08:20:00	$L=40\text{ m}$	~0	0.4-1.0	0.08	0.2

Mis en forme : Exposant

330

331

332 It is interesting to note that, because of their operating modes, the three instruments we
 333 have used provide different information on the SLW clouds that we have synthetized in Table
 334 3. Because the microwave radiometer scans the atmosphere from 0 to 90° zenithal angle to the
 335 East, only overcast clouds and associated LWP can be measured, with no information on the
 336 SLW cloud height. The LIDAR with a 0.4° off-zenith observations is able to detect scattered
 337 and overcast SLW clouds, together with cloud height, with no information on the SLWC or
 338 LWP but, with some limitation in the presence of precipitation and/or low clouds (e.g. liquid
 339 fog) that can alter the observations of cloud above. Finally, the SLWC sonde measures in situ
 340 SLW clouds, thus scattered or overcast clouds together with their heights with an information
 341 on SLWC (thus LWP by vertically integrating SLWC) but there is an increasing horizontal
 342 distance from the station as the flight progresses.

343
 344
 345
 346
 347
 348 **Table 3.** Description of the viewing geometry and comments relative to each instrument used
 349 in our analysis: HAMSTRAD, LIDAR and SLWC sonde.

Mis en forme : Interligne : Double

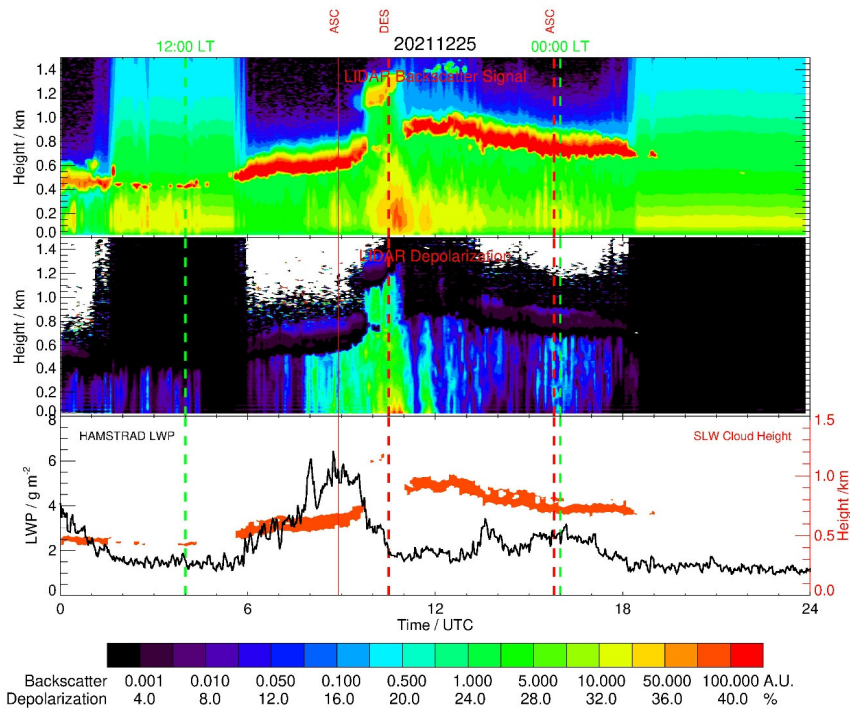
<u>Instruments</u>	<u>Viewing Geometry</u>	<u>Comments</u>
<u>HAMSTRAD</u>	<u>0-90° zenithal angle, to the East</u>	<ul style="list-style-type: none"> - Overcast - Only LWP is measured - No information on the SLW cloud height - Continuous and automated observations
<u>LIDAR</u>	<u>0.4° off-zenith</u>	<ul style="list-style-type: none"> - Scattered and overcast - Information on the SLW cloud height - No information on either SLWC or LWP - Presence of precipitation and/or low clouds can alter the observations of clouds above - Continuous and automated observations

<u>SLWC sonde</u>	<u>In-situ</u>	<ul style="list-style-type: none"> - <u>Increasing horizontal distance from the station as the flight progresses</u> - <u>Scattered and overcast</u> - <u>Information on the SLW cloud height</u> - <u>SLWC is measured along the vertical and LWP can be inferred</u> - <u>Sporadic and manual observations</u>
-------------------	----------------	---

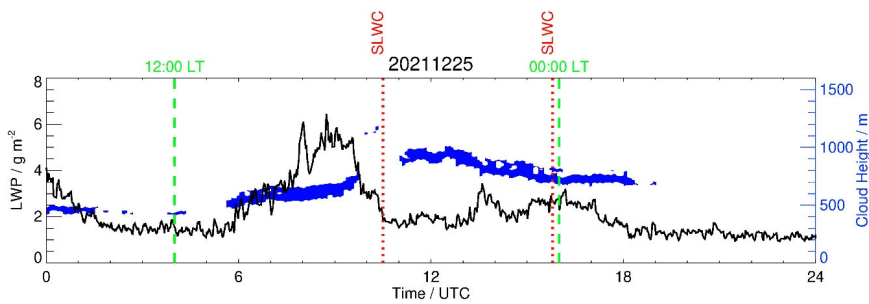
350

351 *4.2. Launches on 25 December 2021*

352 As on 25 December 2021, SLW clouds observed by LIDAR were almost continuously
353 present over Concordia from 00:00 to 19:00 UTC (Figure 2), 2 launches were performed at
354 08:53:15 (L03) and 15:48:51 UTC (L04), from which we will consider ~~both~~ the descending and
355 ascending phases, respectively. For 2 hours before the first launch, SLW clouds were observed
356 by the LIDAR between 500 and 700 m, and during the flight, the SLW clouds were located
357 between 600 and 800 m ~~with some traces of SLW clouds between 1200 and 1300 m~~, while
358 approximately 2 hours after the flight (when the sondes hit the ground in the descending phase)
359 the SLW clouds were located ~~between at 800-900 and 1000-1100-1200 m~~ (see also Table 1).
360 Regarding the second flight, for the 2 hours before the flight, SLW clouds were observed by
361 the LIDAR between 700 and 1000 m and, during the flight, around 700-~~9~~800 m. The first launch
362 was associated with HAMSTRAD-observed LWP values of 1.5-6.0 g m⁻² whereas, for the
363 second flight, it was in the range 1.5-3.0 g m⁻². Note that when the sondes reached the ground
364 at the end of the first launch, the balloon had travelled a distance of about 70 km from the
365 Concordia station after a flight time of 1 h 40 min (Figure 3).



366



367

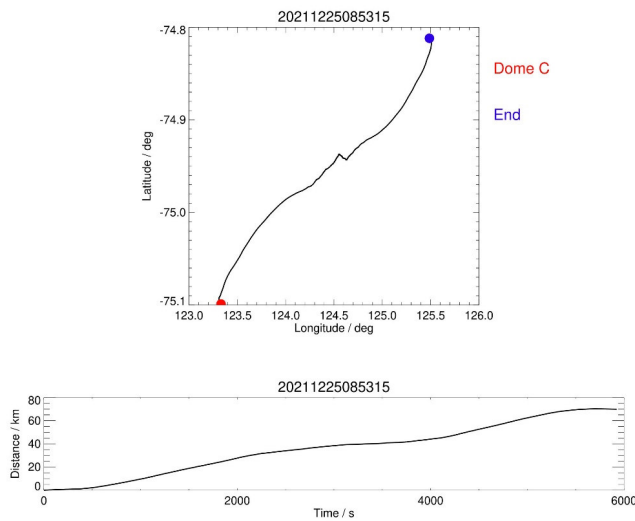
368 **Figure 2:** Diurnal variation on 25 December 2021 (UTC Time) along the vertical of: (top) the
 369 backscatter signal (A.U., Arbitrary Unit); (Center) the depolarization ratio (%) measured by the
 370 LIDAR; (Bottom) the Liquid Water Path (LWP) measured by HAMSTRAD (g m⁻², black solid
 371 line) superimposed with the SLW cloud thickness (red area) derived from the LIDAR
 372 observations (red y-axis on the right). Two vertical green dashed lines indicate 12:00 and 00:00

Mis en forme : Interligne : Double

373 LT. The thick red vertical dashed lines indicate the time when balloon observations with SLWC
374 sondes were performed in ascending (ASC) or descending (DES) phase while the thin red
375 vertical solid line (if any) indicates the launch time corresponding to the observations in the
376 descending phase.

377 **Figure 2:** Diurnal variation of the Liquid Water Path (LWP) measured by HAMSTRAD (g m^{-2} ,
378 black solid line) on 25 December 2021 (UTC Time). Superimposed is the SLW cloud
379 thickness (blue area) derived from the LIDAR observations (blue y axis on the right). Two
380 vertical green dashed lines indicate 12:00 and 00:00 LT. The two red vertical dotted lines
381 indicate the ground landing of the first SLWC sonde (L03 flight) at about 10:30 UTC and the
382 launch of the second SLWC sonde (L04 flight) at about 15:50 UTC, respectively.

383



384

385 **Figure 3:** (Top) Path followed by the meteorological balloon launched on 25 December 2021
386 at 08:53:15 UTC (L03) (red circle) up to the end of the flight (blue circle). (Bottom) Distance
387 travelled (km) as a function of time since launch.

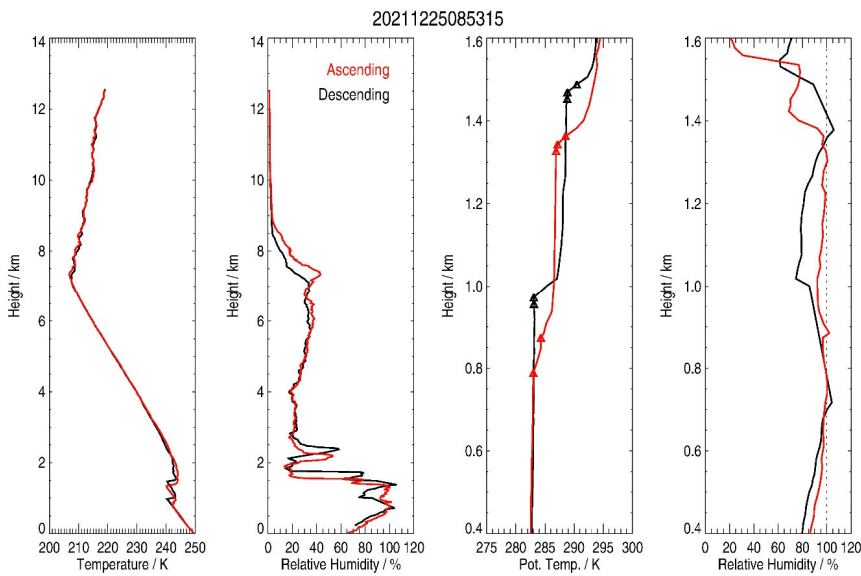
388

389 In general, all the flights reached a top height above 10 km (Figure 4 and Figures S7-14),
390 namely well above the tropopause height (about 7-8 km). This is consistent with previous
391 observations made with meteorological operational Vaisala PTU sondes (Tomasi et al., 2015).
392 The profiles of temperature and relative humidity measured during the whole flight (L03)
393 starting at 08:53:15 UTC are shown in Figure 4 together with the calculated potential
394 temperature and observed relative humidity within the layer [400-1600 m]. Above 2 km, a good
395 consistency between ascending and descending phases is found in temperature profiles within
396 ± 1 K. The relative humidity profiles are within $\pm 5\%$ of each other, except between 7 and 8.5
397 km where they differ by around 10%. Below 2 km, the profiles reflect the impact of the PBL.
398 In ascending phase, the heights of inflection points in potential temperature profiles are found
399 at 800-850 m and 1300-1350 m. In descending phase, they are located at 950-1000 m and 1450-
400 1500 m. Whatever the phase considered, the maximum relative humidity is close to saturation
401 ($U \sim 100\%$) and can even reach supersaturation by 2 to 5 % ($U \sim 102-105\%$) in descending
402 phase. This clearly indicates the presence of clouds. ~~Two~~ Three points need to be underlined.

403 1) The supersaturation highlighted above comes from the actual measurements provided by the
404 Vaisala system with U relative to liquid water. From The Vaisala White paper relative to the
405 RS41 sondes (Vaisala Radiosonde RS41 Measurement Performance, White Paper, Vaisala;
406 available at: [Mis en forme : Police :Italique](https://www.vaisala.com/sites/default/files/documents/WEA-MET-RS41-</u>
407 <u>Performance-White-paper-B211356EN-B-LOW-v3.pdf), the accuracy of temperature and</u>
408 <u>relative humidity are 0.3°C and 4%, respectively below 16 km altitude.</u> 2) The heights of the
409 potential temperature inflection points are higher by ~ 150 m in descending compared with
410 ascending phases. The landing occurred 70 km further out and 1 h 40 min later than the launch
411 (Figure 3). This clearly is a fingerprint of both time and space evolution of the PBL top height
412 around the Concordia station. 3) The presence of a set of two distinct inflection points, namely</p></div><div data-bbox=)

413 two entrainment zones and/or two capping inversion zones where the SLW clouds develop
 414 and/or persist, resemble as if two PBL layers were present above the Concordia station. The
 415 explanation could be that the lowest layer is related to the PBL above Concordia although the
 416 highest layer is either a remnant of the PBL far from Concordia reaching the station through
 417 long-range transport or a fossil layer from the PBL established the day before above the station.
 418 These double layers can be clearly identified on 25 December 2021 at 15:48 UTC (Figure 5),
 419 on 24 January 2022 at 13:51 UTC (Figure S12) and on 28 January 2022 at 06:08 UTC (Figure
 420 S13).

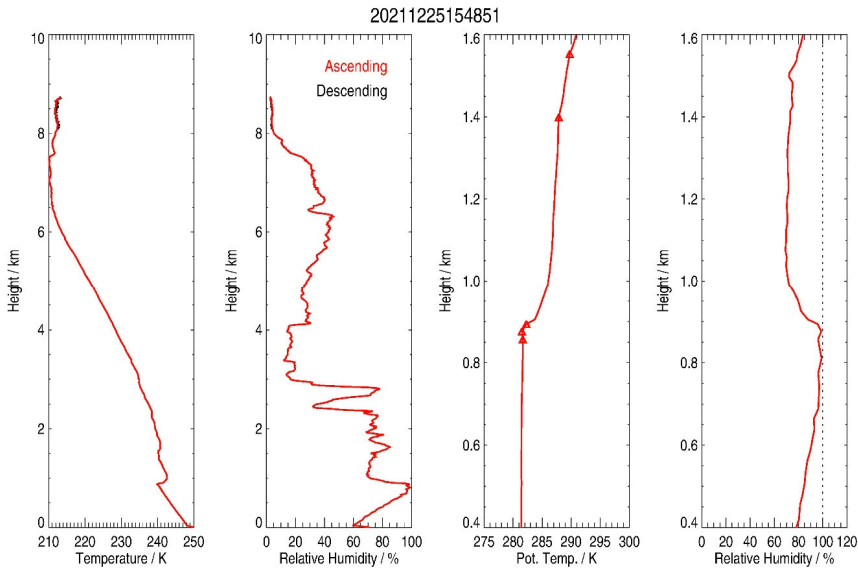
421



422

423 **Figure 4:** (from left to right) Vertical distributions—profiles of: temperature (K), relative
 424 humidity (%) observed by the PTU sonde on 25 December 2021 for a launch at 08:53 UTC in
 425 ascending (red) and descending (black) phases over the entire vertical range, and potential
 426 temperature (K) and relative humidity selected from 400 m to 1600 m height. Red and black
 427 triangles in the vertical profiles of potential temperature highlight the presence of inflection

428 points in the ascending and descending phases, respectively. The vertical dotted line in the right
 429 panel indicates the 100% relative humidity.
 430



431
 432 **Figure 5:** (from left to right) Same as Figure 4 but on 25 December 2021 at 15:48 UTC. Note
 433 that, in descending phase (black), only few observations were available after the balloon
 434 reached the ceiling height.

435
 436 The vertical distributions-profiles of f , df/dt and SLWC associated with the flights L03
 437 and L04 are shown in Figures 6 and 7, respectively. We have also superimposed the vertical
 438 extension of the SLW clouds as observed by the LIDAR within a ± 1 hour window centred on
 439 the launch time (ascending phase) or on the time of the flight end (descending phase) in yellow
 440 or orange, respectively. For both flights, f is rather stable (22.2 and 22.4 Hz, respectively) along
 441 the vertical, with a slight increase between 400 and 600 m during L04. For L03, the
 442 df/dt values are small (± 0.001 Hz s^{-1}) except: 1) between 850 and 1000 m (about -0.005 Hz

443 s^{-1}) where an SLW cloud is estimated from 900 to 1000 m with an SLWC of 0.55 g m^{-3} at 950
444 m and 2) between 1400 and 1500 m (about -0.001 Hz s^{-1}) where an SLW cloud is estimated
445 from 1400 to 1500 m with an SLWC of 0.25 g m^{-3} at 1400 m, well above the estimated $1-\sigma$
446 random error of $0.05\text{-}08 \text{ g m}^{-3}$ (see section 4.3). For L04, the df/dt values are small (± 0.001
447 Hz s^{-1}) except: 1) between 700 and 900 m ($\pm 0.005 \text{ Hz s}^{-1}$) where an SLW cloud is estimated
448 from ~~700-825~~ to ~~900-875~~ m with an SLWC of 0.35 g m^{-3} at 850 m and 2) around 1500 m (about
449 -0.001 Hz s^{-1}) where an SLW cloud is estimated around 1500 m with an SLWC of $0.08\text{-}09 \text{ g m}^{-3}$,
450 very close to the estimated $1-\sigma$ random error of $0.05\text{-}08 \text{ g m}^{-3}$. Note that the df/dt values are
451 high below 500 m, reaching $+0.01 \text{ Hz s}^{-1}$, but this is not related to the presence of SLW, which
452 would translates as negative values of df/dt (see Equation 1).

453 For L03 (Figure 6), two sets of potential temperature inflection points are measured at
454 $H(\theta_{inf}) = 950\text{-}1000$ and $1450\text{-}1500$ m, with no U measurements at these heights. The SLW
455 clouds derived from the SLWC sonde (900-1000 and 1400-1500 m) are located ~~a~~ within the
456 lowest part of $H(\theta_{inf})$ and few meters below. For L04 (Figure 7), two to three potential
457 temperature inflection points are also measured at $H(\theta_{inf}) = 850\text{-}880$, 1400 and 1520 m, with
458 an almost supersaturated atmosphere ($U \sim 100\%$) at 880 m, and high humidity at 1400 m (an
459 elevated $U \sim 75\%$ at 1400 m and $U \sim 80\%$ at 1520 m ($U \sim 80\%$). The SLW clouds derived from
460 the SLWC sonde (700-900 and 1500 m) are located within the lowest part of $H(\theta_{inf})$ and few
461 meters below, as for the L03 flight.

462 The SLW cloud heights derived from the SLWC sonde in L04 (825-875 m) are very
463 consistent with the LIDAR observations (700-900 m). In L03, the SLW cloud at 900-1000 m
464 from the sonde is slightly below the LIDAR observations (800-900 m) in descending phase and
465 slightly above the LIDAR observations (600-800 m) in ascending phase. The SLW cloud at
466 1400-1500 m (L03) is not detected by the LIDAR (except at 1100-1200 m in descending phase
467 for L03). This is probably due to ~~The SLW cloud heights derived from the SLWC sondes in~~

468 L03 and L04 are also consistent with the LIDAR observations (600-800, 800-1000 and 1200-
469 1300 m in L03 and 700-900 m in L04). Note that, in L04, the SLW cloud layer derived from
470 the SLWC sonde at 1450 m is not observed by the LIDAR, probably because the underlying
471 SLW cloud at ~~700-900-900-1000 m~~ that absorbs or reflects most of the LIDAR ~~radiation~~ laser
472 beam, which cannot propagate higher. For L03, the vertically-integrated in the 900-1000 m
473 layer of the SLWC calculated from the sonde data is about 3.7 g m^{-2} , which falls within the
474 minimum-maximum LWP values observed by HAMSTRAD on that day ($2\text{-}6 \text{ g m}^{-2}$) whereas,
475 for L04, the SLWC integrated within the ~~700-825-900-875 m~~ layer is 9.0 g m^{-2} slightly larger
476 than the minimum-maximum values observed by HAMSTRAD ($2\text{-}6 \text{ g m}^{-2}$, see Table 1).

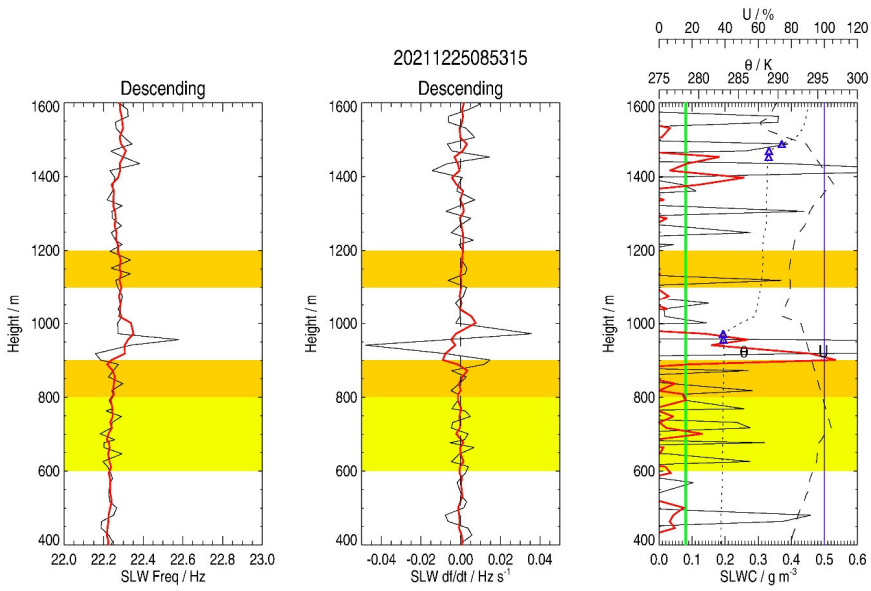
Mis en forme : Exposant

477 An interesting point is to check whether the SLW cloud observed at 900-1000 m by the
478 sonde 70 km away from the station in the descending phase (L03) is connected to the one
479 observed 6000 s earlier by the LIDAR at the station at 600-800 m in the ascending phase, just
480 below the inflection point at 780 m corresponding to the 283-K isentrope. In the ascending
481 phase (Figure S26), the wind direction ($250\pm 20^\circ$) and the wind speed ($18\pm 4 \text{ m s}^{-1}$) in the middle
482 troposphere are consistent with a balloon travelling 70 km in the North-East direction in more
483 than one hour and a half. On the other hand, in the lowermost troposphere (Figures S26 and
484 S27), the wind is orientated to $120\pm 20^\circ$ and the wind speed is much lower ($5\pm 3 \text{ m s}^{-1}$). As a
485 consequence, the probability for the SLW cloud observed by the SLWC sonde in the descending
486 phase to be the one observed by the LIDAR in the ascending phase is very weak. Later on, at
487 15:48:51 (L05), both the LIDAR and the SLWC sonde in the ascending phase observed an SLW
488 cloud in the range 700-900 m, encompassing or just below the inflection points at 850-880 m
489 corresponding to the isentropes 281.5-282 K (Fig. 7). Therefore, it is very likely that the present
490 SLW cloud is a remnant of (or the same as) the one observed 7 hours before over Concordia
491 station within the 283-K isentrope.

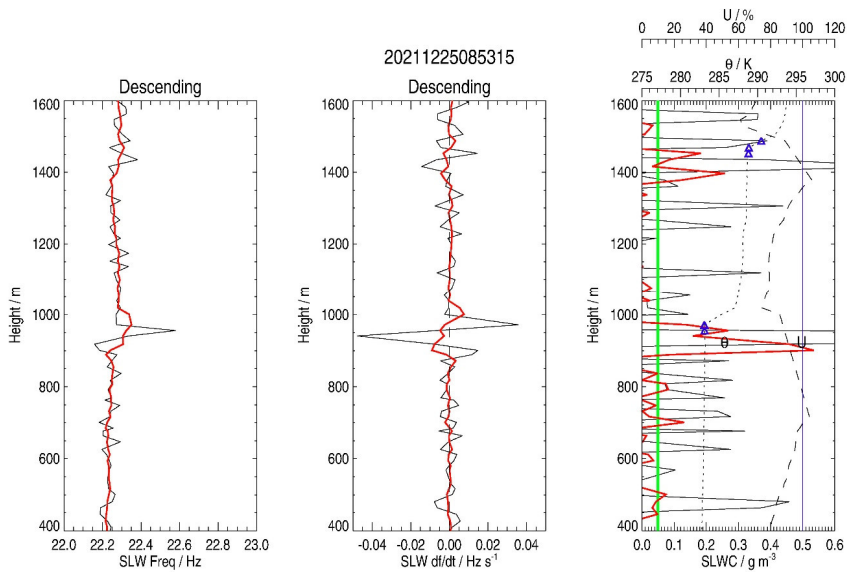
Mis en forme : Exposant

492 ▲

Mis en forme : Anglais (États-Unis)



493



494

495 **Figure 6:** Vertical profiles of: (left) SLWC sonde frequency f (black; Hz), (middle) df/dt (black;

496 Hz s^{-1}); and (right) sonde-calculated SLWC (black; $g\ m^{-3}$) on 25 December 2021 at 10:30 UTC

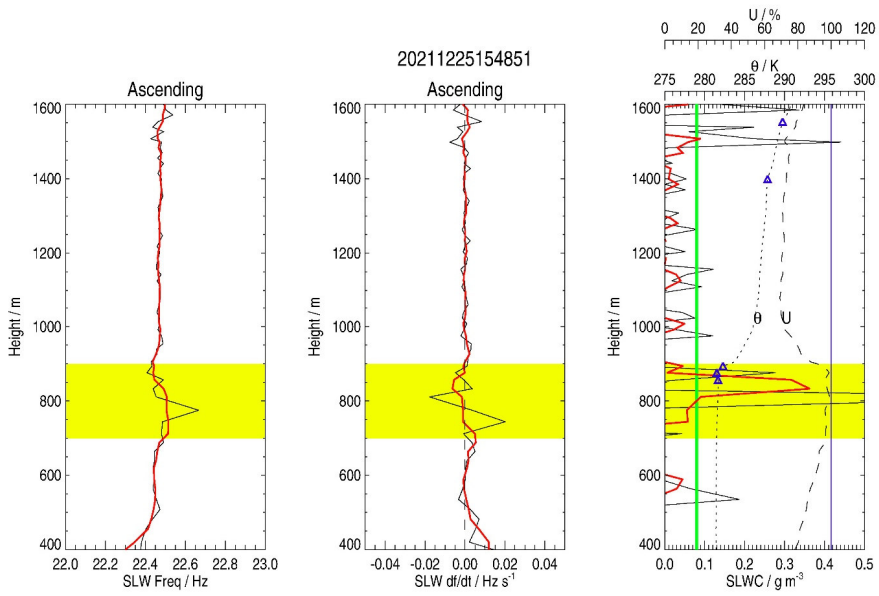
Mis en forme : Interligne : Double

497 (descending phase) for a launch at 08:53:15 UTC. 4-point (20 s) running averages are displayed
498 in red. On the right panel, potential temperature (θ , K) and relative humidity (U, %) are shown
499 as dotted and dashed lines, respectively. Blue triangles represent the height of the potential
500 temperature inflection points. The green vertical line represents the estimated one-sigma error
501 (0.08 g m^{-3}) of the SLWC sonde observations. The blue vertical line indicates the 100% relative
502 humidity. The vertical extension of the SLW clouds as observed by the LIDAR within a ± 1
503 hour window centered on the launch time (ascending phase) or on the time of the flight end
504 (descending phase) is highlighted in yellow or orange, respectively.

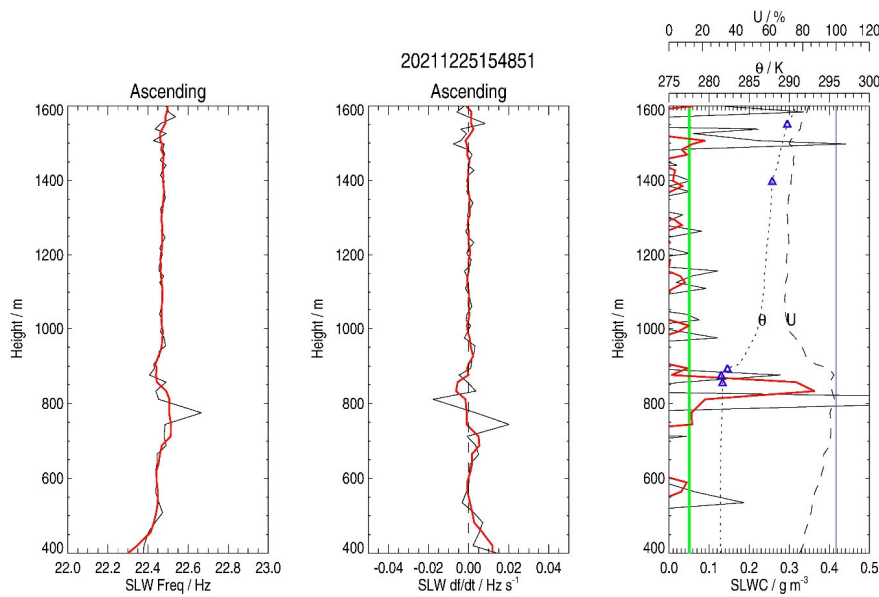
505 **Figure 6:** Vertical distribution of: (left) SLWC sonde frequency f (black; Hz), (middle) df/dt
506 (black; Hz s^{-1}); and (right) sonde-calculated SLWC (black; g m^{-3}) on 25 December 2021 at
507 10:30 UTC (descending phase) for a launch at 08:53:15 UTC. 4 point (20 s) running averages
508 are displayed in red. On the right panel, potential temperature (θ , K) and relative humidity (U,
509 %) are shown as dotted and dashed lines, respectively. Blue triangles represent the height of the
510 potential temperature inflection points. The green vertical line represents the estimated one-
511 sigma error (0.05 g m^{-3}) of the SLWC calculated from the SLWC sonde observations. The blue
512 vertical line indicates the 100% relative humidity.

513

514



515

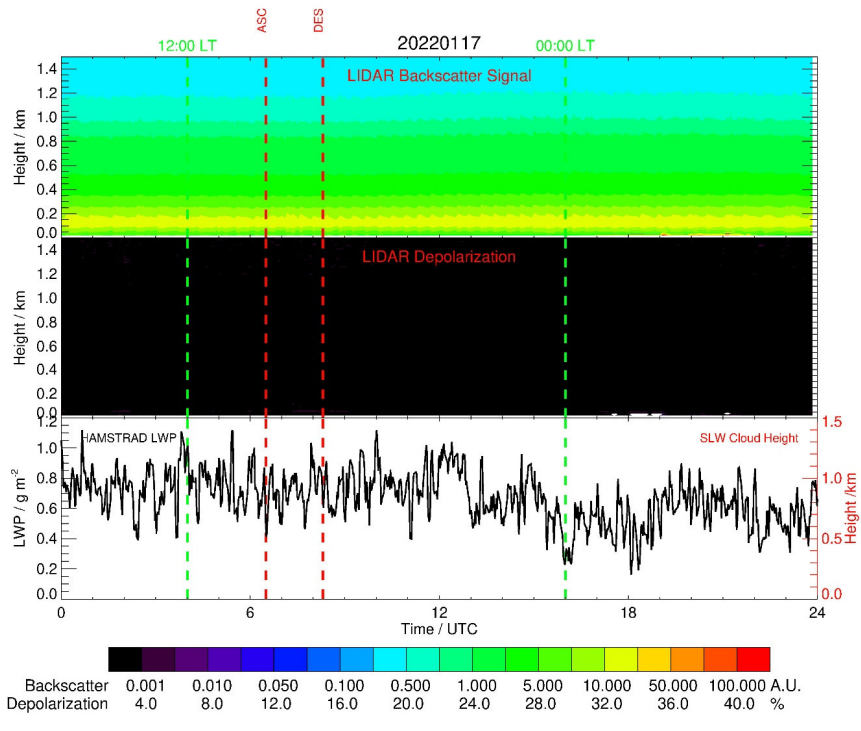


516 **Figure 7:** Same as Figure 6, but for 25 December 2021 at 15:48 UTC (ascending phase).

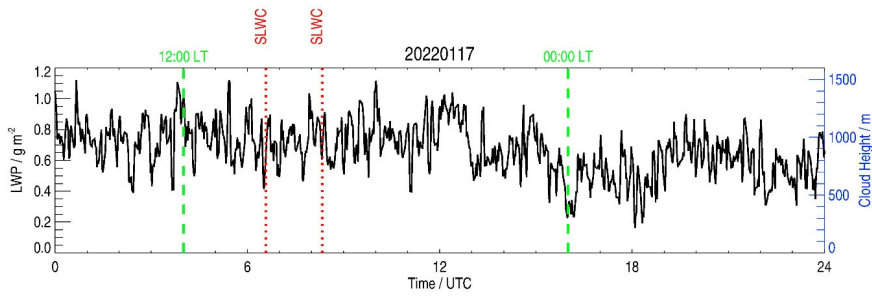
517

518 4.3. Launch on 17 January 2022 (cloud-free period)

519 The launch on 17 January 2022 at 06:15:15 UTC (L11 in ascending and descending phases)
520 was performed in a cloud-free environment throughout the day, as shown by the LIDAR
521 observations (Figures 8), with associated HAMSTRAD-LWP values of 0.4-1.0 g m⁻². This
522 launch was an important test to check the behaviour of the SLWC sonde and to quantify the
523 random error [and the bias](#) associated with the estimation of SLWCs [together with the random](#)
524 [error and the bias in LWP from HAMSTRAD observations](#). Note that when the sondes reached
525 the ground at the end of the flight, the balloon had travelled a distance of approximately 50 km
526 from the Concordia station after a flight time of 1 h 40 min (Figure 9).
527

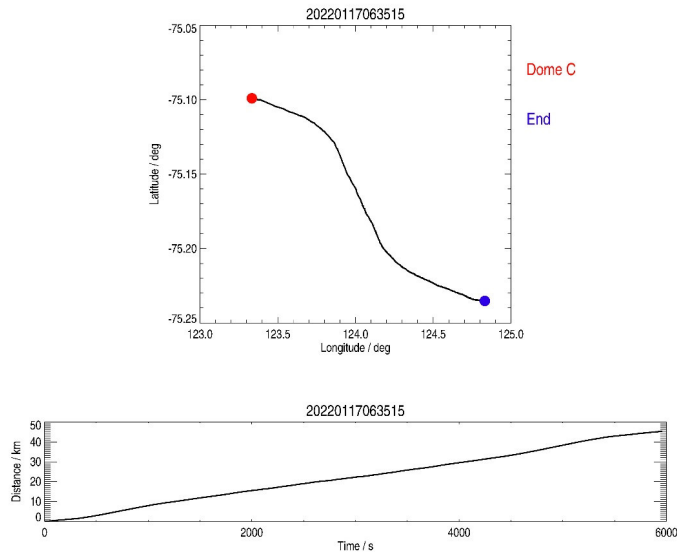


528



529

530 **Figure 8:** Same as Figure 2, but for 17 January 2022, corresponding to a cloud-free condition
 531 period.



532
 533 **Figure 9:** Same as Figure 3, but for the ~~meteorological~~ balloon launched on 17 January 2022
 534 at 07:19:05 UTC.

535
 536 The profiles of f , df/dt and SLWC for flight L11 in its ascending and descending phases
 537 are shown in Figures 10 and 11, respectively. f does not vary much along the vertical in both
 538 flight phases with variations lower than ± 0.05 Hz producing df/dt values- of the order of
 539 ± 0.002 Hz s^{-1} . On average, the SLWC oscillates within ± 0.05 - 08 g m^{-3} . Therefore, we can
 540 estimate the random error in the derived SLWC to be $\sigma = 0.05$ - 08 g m^{-3} without any bias and
 541 conclude that no SLW clouds were observed with the sonde ~~(although some spikes slightly~~
 542 ~~larger than σ are detected at 400 and 1600 m in ascending phase and at 600 and 1200 m in~~
 543 ~~deseending phase)~~. This is consistent with the fact that: 1) the relative humidity is low (U
 544 ranging 10-80%), 2) the LIDAR observations do not show any SLW clouds during the day
 545 (Figure 8) and 3) the HAMSTRAD LWP is small (< 1.0 g m^{-2}). From these HAMSTRAD

546 observations in cloud-free conditions, we can estimate that the LWP RMS error σ is about 0.2

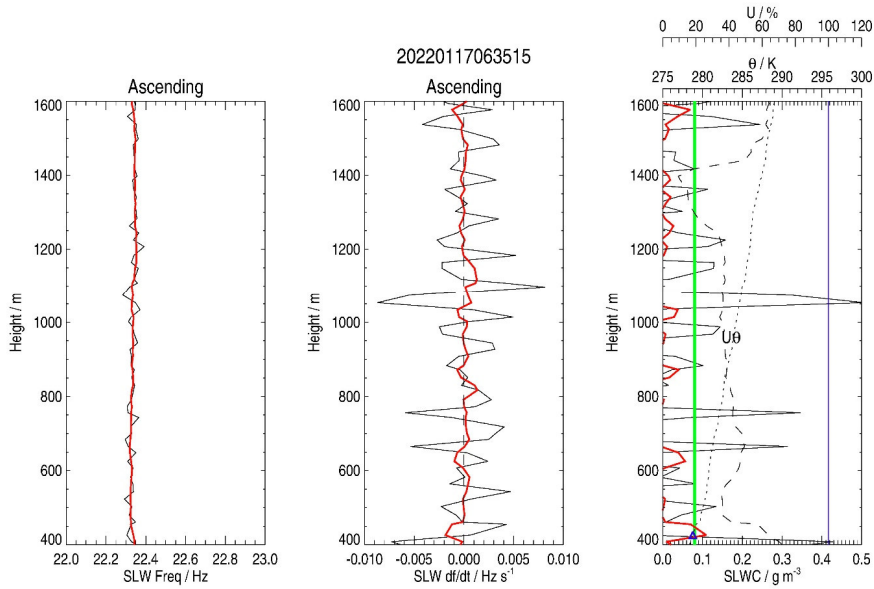
547 g m^{-2} and that the LWP bias is ranging 0.8-1.0 g m^{-2} .

Mis en forme : Police :Italique

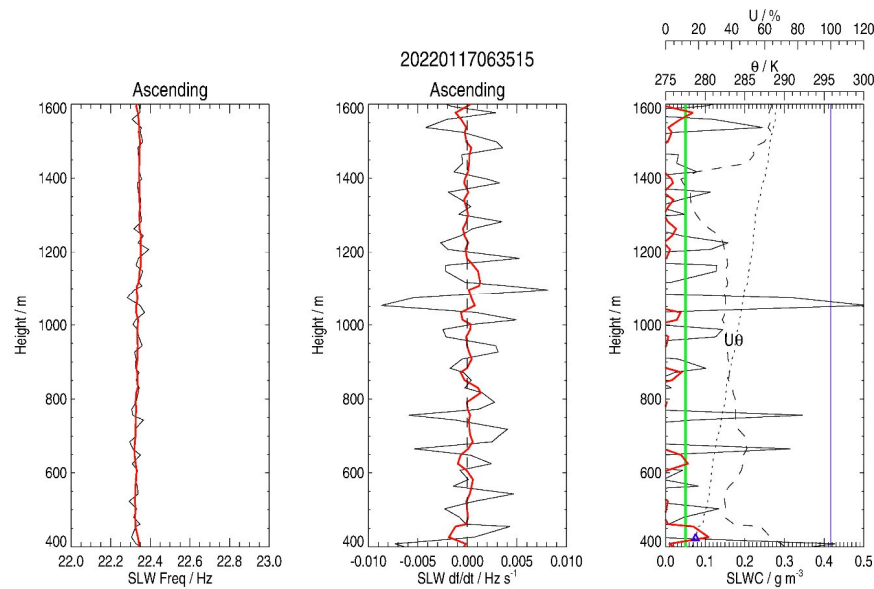
Mis en forme : Exposant

Mis en forme : Exposant

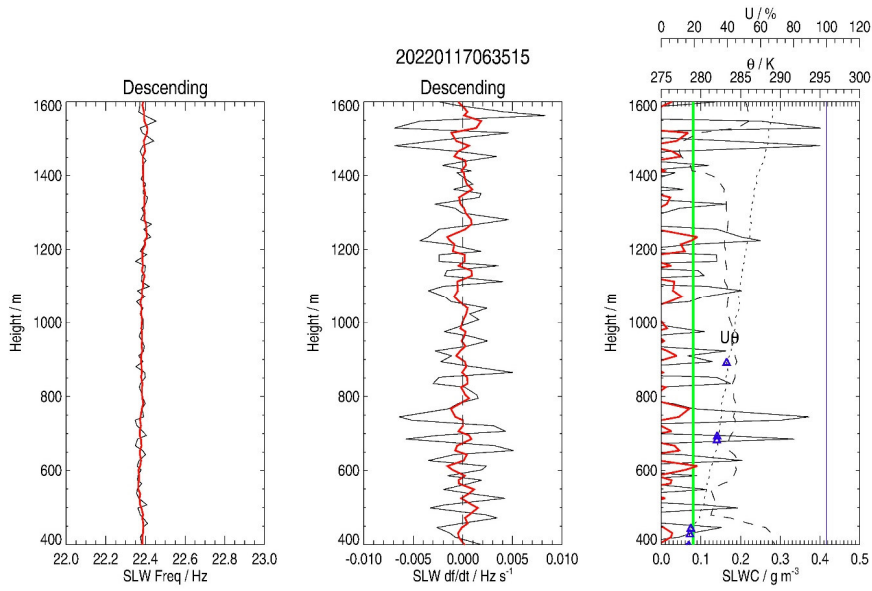
548



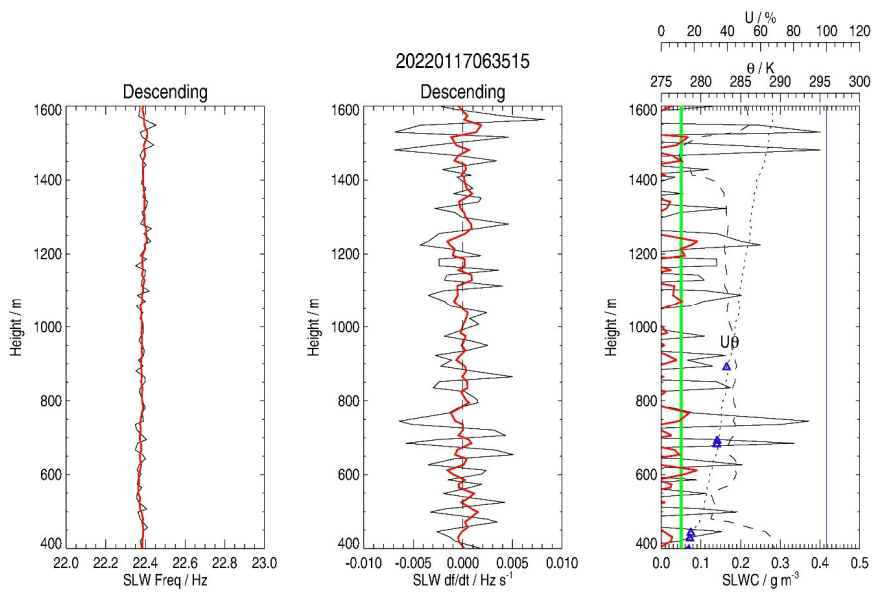
549



550 **Figure 10:** Same as Figure 6, but for 17 January 2022 at 06:35 UTC in ascending phase, in a
551 cloud-free condition.
552



553



554

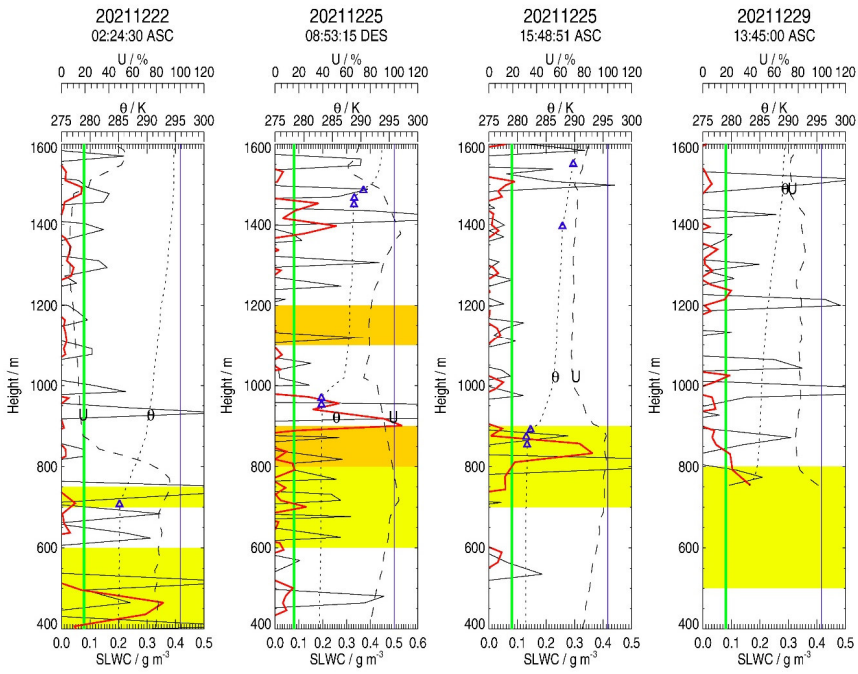
555 **Figure 11:** Same as Figure 6, but for 17 January 2022 at 06:35 UTC in descending phase, in a

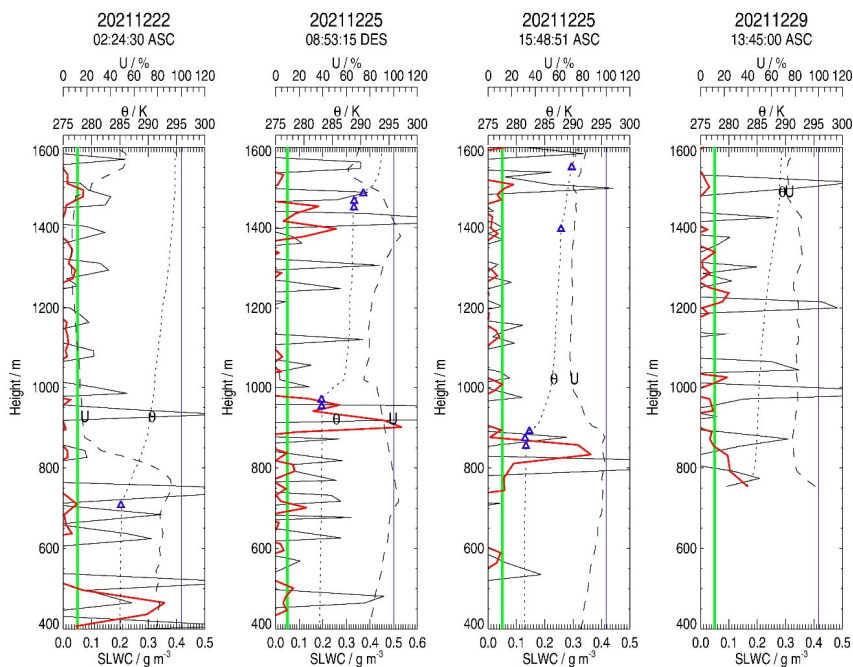
556 cloud-free condition.

557

558 *4.4. Analysis of all the other flights*

559 The first flight (L01) was carried out on 22 December 2021 at 02:24:30 UTC using an
560 unwinder, after the LIDAR detection of an SLW cloud at 400-600 m between 00:00 and 02:00
561 UTC with an LWP of 8-10.5 g m⁻² (Figure S1). Unfortunately, just before the launch, the
562 HAMSTRAD-observed LWP decreased to 1.5 g m⁻², with some remnants of SLW cloud at 500
563 and 650 m. An SLW cloud is estimated by the LIDAR from 400 to 500 m (Figure 12) with an
564 SLWC of 0.35 g m⁻³ at 450 m, well above the estimated 1- σ random error of ~~0.05-0.8~~ g m⁻³.
565 From 400 to 750 m, U increases from 80 to 90% and $H(\theta_{inf})$ is ranging 710-750 m. The LIDAR
566 observed an SLW cloud at ~~750 m~~400-600 m ~~20 min after launch slightly higher than the cloud~~
567 ~~height estimated by~~consistent with the SLWC sonde (400-500 m). The LIDAR SLW cloud at
568 700-750 m is not detected by the SLWC sonde. The integral ~~into~~over the 400-500 m layer of
569 the SLWC measured by the sonde is about 7.4 g m⁻², which is within the minimum-maximum
570 values observed by HAMSTRAD on that day, namely 2-10 g m⁻².





572

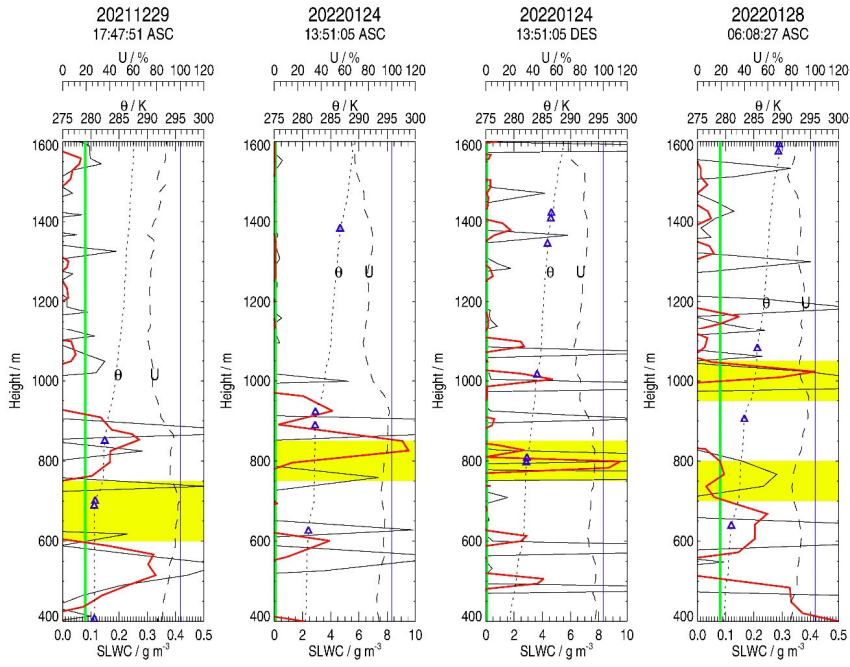
573 **Figure 12:** (from left to right) Profiles of SLWC (black; g m^{-3}) observed on: 22 December 2021
 574 at 02:24 UTC (ascending phase); 25 December 2021 at 10:30 UTC (descending phase) after a
 575 launch at 08:53 UTC; 25 December 2021 at 15:58 UTC (ascending phase) and 29 December
 576 2021 at 13:45 UTC (ascending phase). 4-point (20 s) running averages are displayed in red. The
 577 potential temperature (θ , K) and the relative humidity (U, %) are shown as dotted and dashed
 578 lines, respectively. Blue triangles represent the height of the potential temperature inflection
 579 points. The green vertical line represents the estimated one-sigma error (0.08 g m^{-3}) of the
 580 SLWC calculated from the SLWC sonde observations. The blue vertical line indicates the 100%
 581 relative humidity. The vertical extension of the SLW clouds as observed by the LIDAR within
 582 a ± 1 hour window centered on the launch time (ascending phase) or on the time of the flight
 583 end (descending phase) is highlighted in yellow or orange, respectively. **Figure 12:** (from left
 584 to right) Profiles of SLWC (black; g m^{-3}) observed on: 22 December 2021 at 02:24 UTC

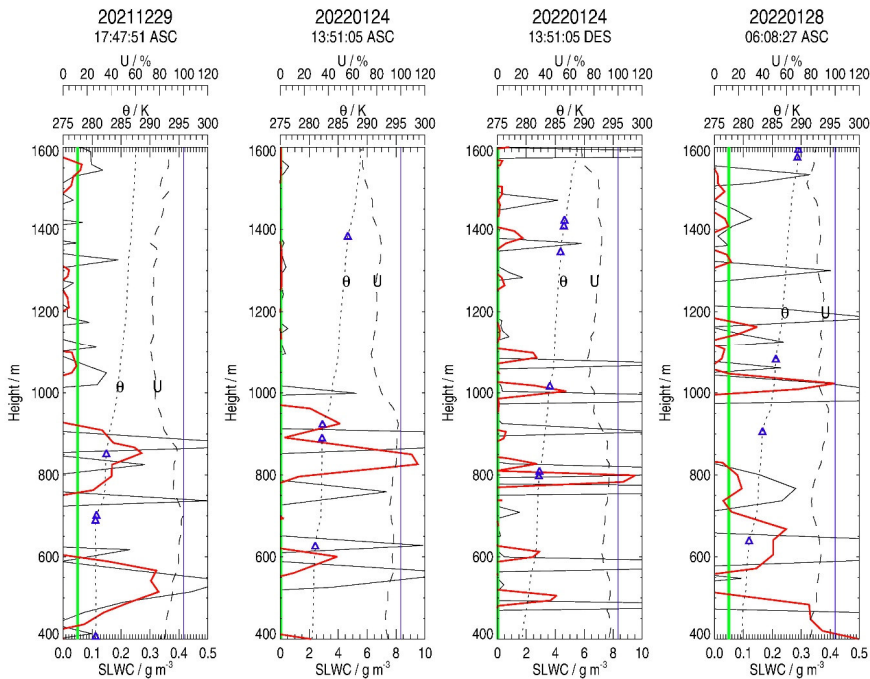
Mis en forme : Normal (Web)

585 (ascending phase); 25 December 2021 at 10:30 UTC (descending phase) after a launch at 08:53
586 UTC; 25 December 2021 at 15:58 UTC (ascending phase) and 29 December 2021 at 13:45
587 UTC (ascending phase). 4 point (20 s) running averages are displayed in red. The potential
588 temperature (θ , K) and the relative humidity (U , %) are shown as dotted and dashed lines,
589 respectively. Blue triangles represent the height of the potential temperature inflection points.
590 The green vertical line represents the estimated one-sigma error (0.05 g m^{-3}) of the SLWC
591 calculated from the SLWC sonde observations. The blue vertical line indicates the 100%
592 relative humidity.

Mis en forme : Anglais (États-Unis)

593
594 To reduce the duration of instability of the SLWC sonde just after the launch of the balloon,
595 from 29 December 2021, we no longer used an unwinder but an unwound string of length $L=40$
596 m (L06 and L07 on 29 December 2021 and L11 on 17 January 2022) or $L=20$ m (L14 on 24
597 January 2022 and L15 on 28 January 2022). We still used a parachute to make observations
598 during the descending phase.





600
 601 **Figure 13:** (from left to right) Same as Figure 12 but on: 29 December 2021 at 17:47 UTC
 602 (ascending phase); 24 January 2022 at 13:51 UTC (ascending phase); 24 January 2022 at 15:30
 603 UTC (descending phase) after a launch at 13:51 UTC and 28 January 2022 at 06:08 UTC
 604 (ascending phase).

605
 606 On 29 December 2021, two launches occurred at 13:45:00 UTC (L06 in ascending phase)
 607 and at 17:47:51 UTC (L07 in ascending phase) after more than 2 hours of SLW clouds observed
 608 by the LIDAR (Figure S3) ~~between 600 and 800 m, which continued during the flight~~. The
 609 launches were associated with HAMSTRAD-LWP values of 1.50-3.50 g m⁻². Note that, on L06,
 610 the PTU and SLWC sondes only started acquiring data above 750 m in the ascending phase.

611 On L06 (Figure 12), an SLW cloud is detected by the sonde between 750 and ~~850-825~~ m
 612 with a maximum of SLWC of 0.16 g m⁻³ and, on L07 (Figure 13), two SLW clouds are

613 estimated, from ~~400-425~~ to 600 m with an SLWC of 0.32 g m^{-3} at 500 m and from 750 to 900
614 m with an SLWC of 0.28 g m^{-3} at 850 m. On L06, the potential temperature inflection point is
615 certainly below the height of 750 m where the sondes started acquiring (~~<750 m~~) with near-
616 saturated air at 750 m and, on L07, two potential temperature inflection points are measured at
617 $H(\theta_{inf}) = 700$ and ~~880-850~~ m, with saturated or near saturated air ($U \sim 100\%$ and $\sim 90\%$,
618 respectively). The SLW clouds derived from the SLWC sonde are in the lowermost part or
619 slightly below $H(\theta_{inf})$. For L06, the LIDAR observed an SLW cloud at 500-800 m
620 encompassing the sonde at 750-825 m. For L07, the LIDAR observed an SLW cloud at 600-
621 750 m between the two cloud layers observed by the sonde at 425-600 and 750-900 m. The
622 upper SLW cloud heights inferred from the SLWC sondes in L06 and L07 are also consistent
623 with the LIDAR observations (600-800 m), but the LIDAR does not detect any cloud between
624 ~~400 and 600 m~~. The amounts of SLWC observed by the sonde and integrated ~~within~~ over the
625 layers 750-~~850-825~~ (L06), ~~400-425~~-600 (L07) and 750-900 m (L07) are about 7.5, 33.2 and 23.9
626 g m^{-2} , respectively, slightly larger (L06) and much larger (L07) than the minimum-maximum
627 values of the LWP observed by HAMSTRAD on that day ($1.0\text{-}3.5 \text{ g m}^{-2}$). Two important points
628 need to be emphasised to explain this excess in SLWCs observed by the sonde on L07. 1) f is
629 not stable along the vertical during the first few hundred meters after launch (Figure S19),
630 contrary to what was observed during the previous flights analysed (sections 4.2 and 4.3). And
631 2) the ascending velocity on this day was lower ($w \sim 3.5 \text{ m s}^{-1}$) than the nominal velocity of the
632 air relative to the vibrating wire ($\sim 5 \text{ m s}^{-1}$).

633 On 24 January 2022, we used both the ascending and descending phases of the flight
634 initiated at 13:51:05 UTC (L14) after more than 2 hours of SLW clouds observed by the LIDAR
635 (Figure S4) near the surface between 0 and 200 m. In fact, an episode of intense liquid fog
636 developed just before the launch. The launch was associated with HAMSTRAD-LWP values
637 of $1.5\text{-}3.0 \text{ g m}^{-2}$. One of the main caveats with liquid fog is that, when it is intense, the LIDAR

638 signal cannot propagate efficiently and the presence of any cloud above the liquid fog layer
639 may not be detected. Note that, when the sondes reached the ground at the end of the flight, the
640 balloon had travelled a distance of about 15 km from the Concordia station during 1 h 25 min
641 of flight (Figure S25). In the ascending phase (L14), two SLW clouds are estimated, around
642 600 m and from 800 to 1000 m (Figure 13). Potential temperature inflection points are detected
643 at $H(\theta_{inf}) = 630$ and 920 m, with air close to saturation ($U \sim 90\text{-}95\%$) and, to a lesser extent, at
644 1400 m. In the descending phase (L15), several spikes of SLW clouds were detected below
645 1200 m, but the ~~two~~ most intense ~~one~~ ~~were~~ ~~was~~ located ~~around 800 and 1000~~ at 775-825 m
646 (Figure 13). The potential temperature inflection points were measured at $H(\theta_{inf}) = ~~800~~810,$
647 ~~1020~~, 1340 and 1420 m, with relative humidity U ranging 85-95%. In both phases, the SLW
648 clouds derived from the SLWC sonde are located in the lowermost part of the
649 entrainment/capping inversion zone. During the flight, the LIDAR measured two SLW clouds
650 ~~around 350~~ at 50-250 and ~~800-750-850~~ m, in addition to near-surface liquid fog. This means
651 that the SLW cloud around 800 m was detected by all the instruments, while an underlying
652 SLW cloud was detected around 600 m by the sondes and much lower (at 350 m) by the LIDAR,
653 slightly below the lowest level where the SLWC sondes start to work well. The SLWCs
654 observed by the sonde and integrated within the layers 800-1000 m (ascending phase) and
655 ~~750-775-850-825~~ m (descending phase) are about 575.3 and ~~1828.79~~ g m⁻², respectively, much
656 larger than the minimum-maximum values observed by HAMSTRAD on that day (1-5 g m⁻²).
657 Two important points must be emphasized in order to explain this excess in SLWC and LWP
658 derived from the sonde in-situ observations ~~by the sonde~~. 1) As far as the flight L14 is
659 concerned, f was not stable along the vertical during the first few hundred meters after launch
660 (Figures S21 and S22), contrary to what was observed during the previous flights analysed
661 (sections 4.2 and 4.3). Above all, the flight was carried out when a liquid fog episode developed
662 over the station. Some ~~ice crystals and/or~~ SLW droplets could well have adhered to the wire of

663 the SLWC sonde before the launch and perturbed the nominal operation of the sonde system,
664 namely the value of the un-iced wire frequency f_0 in eq. (1) ~~vibration frequency~~ and the post-
665 launch stabilization process.

666 The last launch of the summer campaign was performed on 28 January 2022 at 06:08:27
667 UTC (L15 in ascending phase) after more than 2 hours of SLW clouds observed by the LIDAR
668 (Figure S5) at 600-800 m and 900-1000 m. The launch was associated with HAMSTRAD-LWP
669 values of 3.0-3.5 g m⁻². After the launch, the LIDAR detected SLW clouds at about 1000 m.
670 Excluding the large signal at 400-500 m which is probably due to some residual vibrations from
671 the launch (Figure 13), two SLW clouds are estimated by the SLWC sonde from 600 to 800 at
672 550-700 m with an SLWC of 0.25 g m⁻³ at 650 m and around at 1000-1050 m with an SLWC
673 of 0.40 g m⁻³. Three potential temperature inflection points are estimated at $H(\theta_{inf}) = 650, 910$
674 and 1080 m, with U ranging 85-95%. The SLW clouds detected by the SLWC sonde (at ~650
675 and ~1000 m) are well within the entrainment/capping inversion zone and at heights consistent
676 slightly less than with the LIDAR observations (600-700-800 m) or very consistent with the
677 LIDAR measurements (950-1050 and 1000 m), respectively. The SLWC observed by the sonde
678 and integrated within the 600-800-550-700 m and the 950-1000-1050 m layers are about 4.0-13.7
679 and 7.3 g m⁻², respectively, slightly larger than the minimum-maximum values observed by
680 HAMSTRAD on that day (2-5 g m⁻²).

681

682 5. Synthesis and Discussion

683 5.1. SLW cloud

684 Our study reveals that, during the 2021-22 summer campaign at Concordia, the detection
685 of the SLW cloud heights shows high agreement between the remote sensing observations with
686 the LIDAR and the in-situ observations with the SLWC sondes. The clouds are generally
687 located just below the height $H(\theta_{inf})$ of an inflection point in the potential temperature profile,

688 within a layer where the relative humidity U exceeds 80%, sometimes reaching saturation
689 (100%) and in the lowermost part of the entrainment/capping inversion zone depending on the
690 local time. These results are in agreement both with the theory of the diurnal evolution of the
691 ~~planetary boundary layer~~ (PBL), for which boundary-layer clouds develop at the top of the PBL
692 (Stull, 2012), as well as with the first studies carried out at Concordia based only on remote
693 sensing observations (Ricaud et al., 2020). The presence of the SLW clouds is also observed 1)
694 below the height of the inflection point in potential temperature profile during the High-
695 performance Instrumented Airborne Platform for Environmental Research (HIAPER) Pole-to-
696 Pole Observations global transects over the Southern Ocean (Chubb et al., 2013) and 2) around
697 the height of the inflection point in temperature profile above the South Pole station from
698 backscatter LIDAR signal (Lawson and Gettelman, 2014).

699 The SLWC maxima measured by the sondes were ranging 0.2-0.5 g m⁻³ in nominal
700 operations. This is consistent with: 1) the observations performed in the Arctic with the same
701 sondes and with a surface-based AMF3 microwave radiometer (maxima of 0.3-0.4 g m⁻³)
702 attached to a tethered balloon (Dexheimer et al., 2019), 2) in situ airborne observations from
703 HIAPPER (maximum of 0.47 g m⁻³) (Chubb et al., 2013), 3) the 580-s observations from the
704 Southern Ocean Clouds, Radiation, Aerosol Transport Experimental Study (SOCRATES)
705 airborne campaign over the Southern Ocean (maximum of SLWCs of 0.60 g m⁻³) and 4) results
706 from three climate models (maxima of SLWCs ranging from 0.36 to 0.40 g m⁻³) (Yang et al.,
707 2021).

708 It should also be noted that the variations at scales smaller than 100 m in the vertical
709 profiles of the SLWC observations are smoothed out because of: 1) the 5-s integration time of
710 the raw measurements, 2) the method of deriving the SLWC from equation (1) which requires
711 the use of the vertical derivative of f , and 3) the 4-point running average applied to the
712 observations to minimise the effect of large signal frequency undulations on the retrieved

713 SLWC. Therefore, the actual location of the SLW clouds from the SLWC sondes might be
714 slightly displaced compared with the actual location of the entrainment/capping inversion zone
715 derived from the PTU sondes.

716 5.2. Vertically-integrated SLWCs

717 The vertically-integrated SLWCs calculated from in-situ observations were consistent with
718 the minimum-maximum LWPs observed by HAMSTRAD (flights L01 and L03 with
719 unwinders) or slightly larger than the maximum of LWP (flights L04 and L15 with unwinder
720 and a fixed string of $L = 20$ m, respectively). Flight L07 (fixed string of $L = 40$ m) gave a
721 vertically-integrated SLWC greater than that observed by HAMSTRAD by a factor of 5-10,
722 and we can point out that the ascent vertical velocity was certainly too low for the sonde to
723 operate nominally. Finally, for the flight carried out when a [liquid](#) fog episode was present
724 (L14), the vibrating wire of the SLWC sonde was probably affected by this event before launch
725 producing an unrealistically large amount of SLWC during the flight. Furthermore, our best
726 results were obtained with an SLWC sonde attached to the balloon with an unwinder.

727 In nominal operations, LWPs from the sondes were consistent with HAMSTRAD
728 observations ($1-14 \text{ g m}^{-2}$). Nevertheless, LWPs observed over Concordia deep inside the
729 Antarctic Plateau were much less than those observed in the Arctic ($15-40 \text{ g m}^{-2}$ in Dexheimer
730 et al. (2019) and greater than 50 g m^{-2} in Zhang et al. (2019)) and over the coastal Antarctic
731 station of McMurdo ($10-50 \text{ g m}^{-2}$ in Zhang et al. (2019) and $40-60 \text{ g m}^{-2}$ in Hines et al. (2021)).

732 5.3. Quality/sensitivity of the SLWC sonde

733 Flying during a cloud-free period helped to characterize the random RMSE σ associated
734 with the retrieved SLWC. Compared to the other flights carried out during the campaign, the
735 cloud-free flight (L11 with a fixed string of $L = 40$ m) was nominal with a low variability of f
736 during the ascent and descent phases for heights above 400 m, from which we estimated that σ
737 was about $0.05-08 \text{ g m}^{-3}$.

738 The way the balloon is released is a key issue for the stability of the SLWC sonde and
739 needs to be addressed whenever the SLW clouds of interest are near the surface within the PBL.
740 Irrespective of the method used (unwinder or unwound string), during the 2021-22 summer
741 season we were unable to find a way to stabilise the sonde in less than 60 s after launch. One
742 of the main difficulties was that some SLW clouds were located around 400 ± 100 m and, in
743 this case, we were unable to determine whether the variations in the frequency derivatives were
744 due to an instability of the sonde or to a real SLW cloud.

745 Finally, in our opinion, the optimum way to launch the SLWC sonde was to attach it to the
746 balloon with an unwinder although we obtained one scientifically-exploitable flight using an
747 unwound string of length $L=40$ m (L07 on 29 December 2021). However, we have only 9 flights
748 and more flights would be needed to confirm this. We have already highlighted the difficulty
749 of numerical weather prediction models to reproduce the SLW clouds over Concordia, which
750 produces erroneous cloud radiative forcings (Ricaud et al., 2020) along with biased temperature
751 and humidity profiles in the PBL (Ricaud et al., 2023). Therefore, in situ observations, although
752 difficult to deploy, still remain a key tool for improving NWP in these harsh environments.

753

754 **6. Conclusions**

755 The present study intended to observe in situ SLW clouds above the Concordia station by
756 means of sondes sensitive to SLW especially developed by the Anasphere Company. These
757 sondes were attached to meteorological balloons and connected to standard Vaisala PTU sondes
758 during the 2021-2022 summer campaign. These launches were coupled with observations from
759 a backscattered LIDAR providing the nature and height of the clouds, and a microwave
760 radiometer providing the LWP. Over a total of 15 launches, 7 were scientifically exploitable
761 mainly above 400 m agl, a threshold height imposed by the time the SLWC sonde takes to
762 stabilize after the launch.

763 The three main outcomes from our analysis are:

764 a) The in-situ observations of SLW clouds with SLWC sondes at Concordia station in
765 Antarctica are the first observations so far in Antarctica with a SLWC sonde. The location in
766 height of the SLW clouds observed by the SLWC sonde is consistent with the profiles of
767 humidity and temperature (and the deduced inflection points).

768 b) On average, the heights of the SLW clouds as observed by in-situ sondes and remonte-
769 sensing LIDAR are consistent.

770 c) The Liquid Water Path (vertically-integrated supercooled liquid water content, SLWC)
771 deduced from the sonde observations generally equals or is greater than LWP remotely sensed
772 by a ground-based microwave radiometer.

Mis en forme : Anglais (États-Unis)

773 ~~In general, during nominal operations, the SLWC sondes detected SLW clouds in a vertical~~
774 ~~domain consistent with LIDAR observations, and the LWP values either obtained by~~
775 ~~HAMSTRAD or vertically-integrated from the SLWC values calculated from the sonde~~
776 ~~observations were consistent in spite of their-its low values ($< 10 \text{ g m}^{-2}$). Unfortunately, on some~~
777 occasions far from nominal operation (surface liquid fog, low vertical ascent of the balloon),
778 the ~~sonde~~-vertically-integrated SLWCs ~~from the sonde~~ were overestimated by a factor of 5-10
779 compared to the HAMSTRAD LWPs.

780 Although the vertical ~~resolution-sensitivity~~ of the SLWC observations is around 100 m due
781 to the methodology employed (4-point running average of 5-s integration time) and the vertical
782 ascent of 5 m s^{-1} , the SLW clouds were observed in a layer close to saturation ($U > 80\%$) or
783 saturated ($U \sim 100-105\%$) just below or at the lowermost part of the entrainment zone or capping
784 inversion zone which exists at the top of the PBL and is characterized by an inflection point in
785 the potential temperature vertical profiles. Consequently, our results are consistent with the
786 theoretical view that SLW clouds form and pertain at the top of the PBL.

787 Because of the positive scientific results obtained during this first balloon campaign and
788 since the second campaign in 2022-2023 was technologically successful using a VTOL drone,
789 we forecast a new summer campaign to probe the PBL with an SLWC sonde aboard a drone.
790 The main advantages of the drone compared with the meteorological balloon are that: 1) it can
791 fly every day or even twice a day with the same SLWC sonde onboard minimizing the number
792 of SLWC and PTU sondes used, ~~and~~ 2) it does not require Helium gas that is coming to be more
793 and more difficult and costly with time and 3) it allows us to explore the horizontal variability
794 of the clouds that overperforms the single location of the vertical profiles provided by ground-
795 based instruments.
796

797 **Data availability**

798 HAMSTRAD data are available at <http://www.cnrm.meteo.fr/spip.php?article961&lang=en>
799 (Ricaud, 2024). The tropospheric depolarization LIDAR data are reachable at
800 <http://lidarmax.altervista.org/lidar/home.php> (Del Guasta, 2024). Radiosondes are available at
801 http://www.climantartide.it/dataaccess/RDS_CONCORDIA/index.php?lang=en (Grigioni,
802 2024).
803

804 **Author contribution**

805 PR, MDG, GC, AR, PG and JB provided the observational data. PR developed the
806 methodology with the help of all co-authors. All the co-authors participated in the data analysis
807 and in the data interpretation. PR prepared the manuscript with contributions from all co-
808 authors.
809

810 **Competing interests**

811 The authors declare that they have no conflict of interest.

812

813 **Acknowledgements**

814 The present research project Water Budget over Dome C (H₂O-DC) has been approved by
815 the Year of Polar Prediction (YOPP) international committee. The permanently staffed
816 Concordia station is jointly operated by Institut polaire français Paul-Emile Victor (IPEV) and
817 the Italian Programma Nazionale Ricerche in Antartide (PNRA). The tropospheric LIDAR
818 operates at Dome C from 2008 within the framework of several Italian national (PNRA)
819 projects. We would like to thank all the winterover personnel who worked at Dome C on the
820 different projects. [Finally, we would like to thank the two anonymous reviewers for their](#)
821 [beneficial comments.](#)

822

823 **Financial support**

824 The HAMSTRAD programme 910 and the SLW-CLOUDS programme 1247 were
825 supported by IPEV, the Institut National des Sciences de l'Univers (INSU)/Centre National de
826 la Recherche Scientifique (CNRS), Météo-France, and the Centre National d'Etudes Spatiales
827 (CNES).

828

829 **References**

830 [Bain, M. and Gayet, J.F.: Aircraft measurements of icing in supercooled and water droplet/ice](#)
831 [crystal clouds. Journal of Applied Meteorology, 21, 631-641,](#)
832 [https://www.jstor.org/stable/26180452, 1982.](https://www.jstor.org/stable/26180452)

833 Bromwich, D. H., Nicolas, J. P., Hines, K. M., Kay, J. E., Key, E. L., Lazzara, Lubin, D.,
834 McFarquhar, G. M., Gorodetskaya, I. V., Grosvenor, D. P., Lachlan-Cope, T., and van
835 Lipzig, N. P. M.: Tropospheric clouds in Antarctica, Rev. Geophys., 50, RG1004,
836 <https://doi.org/10.1029/2011RG000363>, 2012.

837 Bromwich, D. H., Otieno, F. O., Hines, K. M., Manning, K. W., and Shilo, E.: Comprehensive
838 evaluation of polar weather research and forecasting model performance in the Antarctic, J.
839 Geophys. Res.-Atmos., 118, 274–292, 2013.

840 Chubb, T.H., Jensen, J.B., Siems, S.T. and Manton, M.J.: In situ observations of supercooled
841 liquid clouds over the Southern Ocean during the HIAPER pole-to-pole observation
842 campaigns. *Geophysical Research Letters*, 40(19), 5280-5285, 2013.

843 Cossich, W., Maestri, T., Magurno, D., Martinazzo, M., Di Natale, G., Palchetti, L., Bianchini,
844 G., and Del Guasta, M.: Ice and mixed-phase cloud statistics on the Antarctic Plateau,
845 Atmos. Chem. Phys., 21, 13811–13833, <https://doi.org/10.5194/acp-21-13811-2021>, 2021.

846 Del Guasta, M.: LIDAR – INO CNR in Antartide, INO-CNR [data set],
847 <http://lidarmax.altervista.org/lidar/home.php>, last access: 17 January 2024.

848 Dexheimer, D., M. Airey, E. Roesler, C. Longbottom, K. Nicoll, S. Kneifel, F. Mei, R. G.
849 Harrison, G. Marlton, and P. D. Williams: Evaluation of ARM tethered-balloon system
850 instrumentation for supercooled liquid water and distributed temperature sensing in mixed-
851 phase Arctic clouds, Atmos. Meas. Tech., 12, 6845–6864, [https://doi.org/10.5194/amt-12-](https://doi.org/10.5194/amt-12-6845-2019)
852 6845-2019, 2019.

853 Engdahl, B.J.K., Thompson, G. and Bengtsson, L.: Improving the representation of supercooled
854 liquid water in the HARMONIE-AROME weather forecast model. *Tellus A: Dynamic*
855 *Meteorology and Oceanography*, 72(1), 1-18,
856 <https://doi.org/10.1080/16000870.2019.1697603>, 2020.

857 [Fogt, R.L. and Bromwich, D.H.: Atmospheric moisture and cloud cover characteristics forecast](#)
858 [by AMPS. *Weather and forecasting*, 23\(5\), 914-930, 2008.](#)

859 Grazioli, J., Genthon, C., Boudevillain, B., Duran-Alarcon, C., Del Guasta, M., Madeleine, J.-
860 B., and Berne, A.: Measurements of precipitation in Dumont d’Urville, Adélie Land, East

861 Antarctica, *The Cryosphere*, 11, 1797–1811, <https://doi.org/10.5194/tc-11-1797-2017>,
862 2017.

863 Grigioni, P.: Antarctic Meteo-Climatological Observatory, IAMCO [data set],
864 http://www.climantartide.it/dataaccess/RDS_CONCORDIA/index.php?lang=en, last
865 access: 17 January 2024.

866 Grosvenor, D. P., Choularton, T. W., Lachlan-Cope, T., Gallagher, M. W., Crosier, J., Bower,
867 K. N., Ladkin, R. S., and Dorsey, J. R.: In-situ aircraft observations of ice concentrations
868 within clouds over the Antarctic Peninsula and Larsen Ice Shelf, *Atmos. Chem. Phys.*, 12,
869 11275–11294, <https://doi.org/10.5194/acp-12-11275-2012>, 2012.

870 Hennemuth, B., and Lammert, A.: Determination of the atmospheric boundary layer height
871 from radiosonde and lidar backscatter. *Boundary-Layer Meteorology*, 120, 181-200,
872 <https://doi.org/10.1007/s10546-005-9035-3>, 2006.

873 Hines, K.M., Bromwich, D.H., Silber, I., Russell, L.M. and Bai, L.: Predicting Frigid Mixed-
874 Phase Clouds for Pristine Coastal Antarctica. *Journal of Geophysical Research:*
875 *Atmospheres*, 126(23), p.e2021JD035112, 2021.

876 Hogan, R. J. and Illingworth, A. J.: The effect of specular reflection on spaceborne lidar
877 measurements of ice clouds, Report of the ESA Retrieval algorithm for EarthCARE project,
878 5 pp., 2003.

879 King, J. C., Argentini, S. A., and Anderson, P. S.: Contrasts between the summertime surface
880 energy balance and boundary layer structure at Dome C and Halley stations, Antarctica, *J.*
881 *Geophys. Res.-Atmos.*, 111, D02105, <https://doi.org/10.1029/2005JD006130>, 2006.

882 King, J. C., Gadian, A., Kirchgassner, A., Kuipers Munneke, P., Lachlan-Cope, T. A., Orr, A.,
883 Reijmer, C., Broeke, M. R., van Wessem, J. M., and Weeks, M.: Validation of the
884 summertime surface energy budget of Larsen C Ice Shelf (Antarctica) as represented in

885 three high-resolution atmospheric models, *J. Geophys. Res.-Atmos.*, 120, 1335–1347,
886 <https://doi.org/10.1002/2014JD022604>, 2015.

887 Lachlan-Cope, T.: Antarctic clouds, *Polar Res.*, 29, 150–158, 2010.

888 Lachlan-Cope, T., Listowski, C., and O’Shea, S.: The microphysics of clouds over the Antarctic
889 Peninsula – Part 1: Observations, *Atmos. Chem. Phys.*, 16, 15605–15617,
890 <https://doi.org/10.5194/acp-16-15605-2016>, 2016.

891 Lawson, R. P. and Gettelman, A.: Impact of Antarctic mixed-phase clouds on climate, *P. Natl.*
892 *Acad. Sci. USA*, 111, 18156–18161, 2014.

893 Lemus, L., Rikus, L., Martin, C., and Platt, R.: Global cloud liquid water path simulations. *J.*
894 *Climate*, 10(1), 52-64, 1997.

895 Lenaerts, J. T., Van Tricht, K., Lhermitte, S. and L’Ecuyer, T. S.: Polar clouds and radiation in
896 satellite observations, reanalyses, and climate models, *Geophysical Research Letters*, 44(7),
897 3355-3364, 2017.

898 Listowski, C. and Lachlan-Cope, T.: The microphysics of clouds over the Antarctic Peninsula
899 – Part 2: modelling aspects within Polar WRF, *Atmos. Chem. Phys.*, 17, 10195–10221,
900 <https://doi.org/10.5194/acp-17-10195-2017>, 2017.

901 Listowski, C., Delanoë, J., Kirchgaessner, A., Lachlan-Cope, T., and King, J.: Antarctic clouds,
902 supercooled liquid water and mixed phase, investigated with DARDAR: geographical and
903 seasonal variations, *Atmos. Chem. Phys.*, 19, 6771–6808, [https://doi.org/10.5194/acp-19-](https://doi.org/10.5194/acp-19-6771-2019)
904 [6771-2019](https://doi.org/10.5194/acp-19-6771-2019), 2019.

905 [Lozowski, E.P., Stallabrass, J.R. and Hearty, P.F.: The icing of an unheated, nonrotating](#)
906 [cylinder. Part I: A simulation model. *Journal of applied meteorology and climatology*,](#)
907 [22\(12\), 2053-2062, \[https://doi.org/10.1175/1520-\]\(https://doi.org/10.1175/1520-0450\(1983\)022%3C2053:TIOAUN%3E2.0.CO;2\)](#)
908 [0450\(1983\)022%3C2053:TIOAUN%3E2.0.CO;2, 1983.](#)

909 Lubin, D., Chen, B., Bromwich, D. H., Somerville, R. C., Lee, W. H., and Hines, K. M.: The
910 Impact of Antarctic Cloud Radiative Properties on a GCM Climate Simulation, *J. Climate*,
911 11, 447-462, 1998.

912 Mishchenko, M. I., Hovenier, J. W., and Travis, L. D. (Eds.): *Light Scattering by Nonspherical*
913 *Particles: Theory, Measurements, and Applications*, Academic Press, chap. 14, 393–416,
914 2000.

915 O’Shea, S. J., Choulaton, T. W., Flynn, M., Bower, K. N., Gallagher, M., Crosier, J., Williams,
916 P., Crawford, I., Fleming, Z. L., Listowski, C., Kirchaessner, A., Ladkin, R. S., and
917 Lachlan-Cope, T.: In situ measurements of cloud microphysics and aerosol over coastal
918 Antarctica during the MAC campaign, *Atmos. Chem. Phys.*, 17, 13049–13070,
919 <https://doi.org/10.5194/acp-17-13049-2017>, 2017.

920 Ricaud, P.: HAMSTRAD, CNRM [data set],
921 <http://www.cnrm.meteo.fr/spip.php?article961&lang=en>, last access: 17 January 2024.

922 Ricaud, P., Gabard, B., Derrien, S., Chaboureaud, J.-P., Rose, T., Mombauer, A. and Czekala,
923 H.: HAMSTRAD-Tropo, A 183-GHz Radiometer Dedicated to Sound Tropospheric Water
924 Vapor Over Concordia Station, Antarctica, *IEEE T. Geosci. Remote*, 48, 1365–1380, doi:
925 10.1109/TGRS.2009.2029345, 2010.

926 Ricaud, P., Bazile, E., del Guasta, M., Lanconelli, C., Grigioni, P., and Mahjoub, A.: Genesis
927 of diamond dust, ice fog and thick cloud episodes observed and modelled above Dome C,
928 Antarctica, *Atmos. Chem. Phys.*, 17, 5221-5237, [https://doi.org/10.5194/acp-17-5221-](https://doi.org/10.5194/acp-17-5221-2017)
929 2017, 2017.

930 Ricaud, P., Del Guasta, M., Bazile, E., Azouz, N., Lupi, A., Durand, P., Attié, J.-L., Veron, D.,
931 Guidard, V., and Grigioni, P.: Supercooled liquid water cloud observed, analysed, and
932 modelled at the top of the planetary boundary layer above Dome C, Antarctica, *Atmos.*
933 *Chem. Phys.*, 20, 4167–4191, <https://doi.org/10.5194/acp-20-4167-2020>, 2020.

934 Ricaud, P., Medina, P., Durand, P., Attié, J.L., Bazile, E., Grigioni, P., Guasta, M.D. and Pauly,
935 B.: In Situ VTOL Drone-Borne Observations of Temperature and Relative Humidity over
936 Dome C, Antarctica. *Drones*, 7(8), 532, <https://doi.org/10.3390/drones7080532>, 2023.

937 Ricaud, P., Del Guasta, M., Lupi, A., Roehrig, R., Bazile, E., Durand, P., Attié, J.-L., Nicosia,
938 A., and Grigioni, P.: Supercooled liquid water clouds observed over Dome C, Antarctica:
939 temperature sensitivity and cloud radiative forcing. *Atmos. Chem. Phys.*, 24, 613–630,
940 <https://doi.org/10.5194/acp-24-613-2024>, 2024.

941 Serke, D., E. Hall, J. Bognar, A. Jordan, S. Abdo, K. Baker, T. Seitel, M. Nelson, R. Ware, F.
942 McDonough, and M. Politovich: Supercooled liquid water content profiling case studies
943 with a new vibrating wire sonde compared to a ground-based microwave radiometer,
944 *Atmospheric Research*, 149, 77–87, <http://dx.doi.org/10.1016/j.atmosres.2014.05.026>,
945 2014.

946 Stull, R. B.: *An introduction to boundary layer meteorology*, Vol. 13, Springer Science &
947 Business Media, 2012.

948 Tomasi, C., Petkov, B., Mazzola, M., Ritter, C., di Sarra, A., di Iorio, T., and del Guasta, M.:
949 Seasonal variations of the relative optical air mass function for background aerosol and thin
950 cirrus clouds at Arctic and Antarctic sites, *Remote Sensing*, 7(6), 7157-7180, 2015.

951 Yang, C. A., Diao, M., Gettelman, A., Zhang, K., Sun, J., McFarquhar, G., and Wu, W.: Ice
952 and supercooled liquid water distributions over the Southern Ocean based on in situ
953 observations and climate model simulations. *Journal of Geophysical Research:*
954 *Atmospheres*, 126, e2021JD036045. <https://doi.org/10.1029/2021JD036045>, 2021.

955 Young, G., Lachlan-Cope, T., O’Shea, S. J., Dearden, C., Listowski, C., Bower, K. N.,
956 Choularton, T. W., and Gallagher, M. W.: Radiative effects of secondary ice enhancement
957 in coastal Antarctic clouds, *Geophys. Res. Lett.*, 46, 2312–2321,
958 <https://doi.org/10.1029/2018GL080551>, 2019.

959 Zhang, D., Vogelmann, A., Kollias, P., Luke, E., Yang, F., Lubin, D. and Wang, Z.: Comparison
960 of Antarctic and Arctic single-layer stratiform mixed-phase cloud properties using ground-
961 based remote sensing measurements. *Journal of Geophysical Research: Atmospheres*,
962 *124*(17-18), 10186-10204, <https://doi.org/10.1029/2019JD030673>, 2019.
963